

Formation of massive black holes in rapidly growing pre-galactic gas clouds

John H. Wise^{1*}, John A. Regan², Brian W. O'Shea^{3,4}, Michael L. Norman^{5,6}, Turlough P. Downes² & Hao Xu^{5,6,7}

The origin of the supermassive black holes that inhabit the centres of massive galaxies remains unclear^{1,2}. Direct-collapse black holes—remnants of supermassive stars, with masses around 10,000 times that of the Sun—are ideal seed candidates^{3–6}. However, their very existence and their formation environment in the early Universe are still under debate, and their supposed rarity makes modelling their formation difficult^{7,8}. Models have shown that rapid collapse of pre-galactic gas (with a mass infall rate above some critical value) in metal-free haloes is a requirement for the formation of a protostellar core that will then form a supermassive star^{9,10}. Here we report a radiation hydrodynamics simulation of early galaxy formation^{11,12} that produces metal-free haloes massive enough and with sufficiently high mass infall rates to form supermassive stars. We find that pre-galactic haloes and their

associated gas clouds that are exposed to a Lyman–Werner intensity roughly three times the intensity of the background radiation and that undergo at least one period of rapid mass growth early in their evolution are ideal environments for the formation of supermassive stars. The rapid growth induces substantial dynamical heating^{13,14}, amplifying the Lyman–Werner suppression that originates from a group of young galaxies 20 kiloparsecs away. Our results strongly indicate that the dynamics of structure formation, rather than a critical Lyman–Werner flux, is the main driver of the formation of massive black holes in the early Universe. We find that the seeds of massive black holes may be much more common than previously considered in overdense regions of the early Universe, with a co-moving number density up to 10^{-3} per cubic megaparsec.

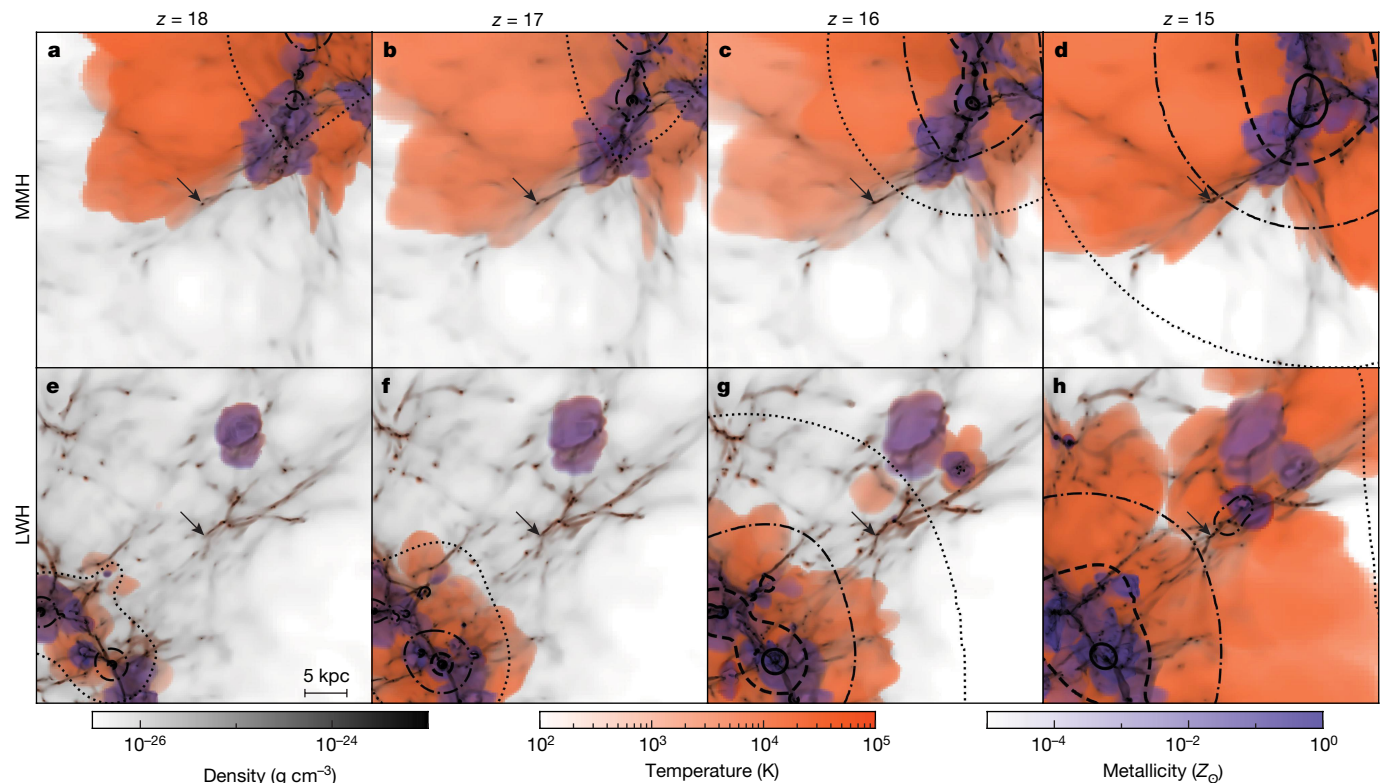


Fig. 1 | Thermal and chemical evolution of the immediate pre-galactic environment. a–h, Projections of the temperature (orange), metallicity (blue; Z_{\odot} is the metallicity of the Sun) and gas density (black) of a region 40 kpc across and with a depth of 8 kpc centred on the MMH (a–d) and the LWH (e–h). The MMH and LWH are indicated by arrows. The heated and metal-enriched volumes around early galaxies and population III stars

grow from $z = 18$ to $z = 15$ (62 Myr). The dotted, dash-dotted, dashed and solid contours indicate where the average Lyman–Werner flux is $1J_{21}$, $3J_{21}$, $10J_{21}$ and $30J_{21}$. Both candidate haloes, which host the formation of massive black holes, have $3J_{21}$, are just outside of the cosmological H II region and are still unaffected by any external metal-rich winds.

¹Center for Relativistic Astrophysics, School of Physics, Georgia Institute of Technology, Atlanta, GA, USA. ²Centre for Astrophysics and Relativity, School of Mathematical Sciences, Dublin City University, Dublin, Ireland. ³Department of Computational Mathematics, Science and Engineering, Michigan State University, East Lansing, MI, USA. ⁴Department of Physics and Astronomy, Michigan State University, East Lansing, MI, USA. ⁵Center for Astrophysics and Space Sciences, University of California, San Diego, CA, USA. ⁶San Diego Supercomputer Center, San Diego, CA, USA. ⁷IBM, Poughkeepsie, NY, USA. *e-mail: jwise@gatech.edu

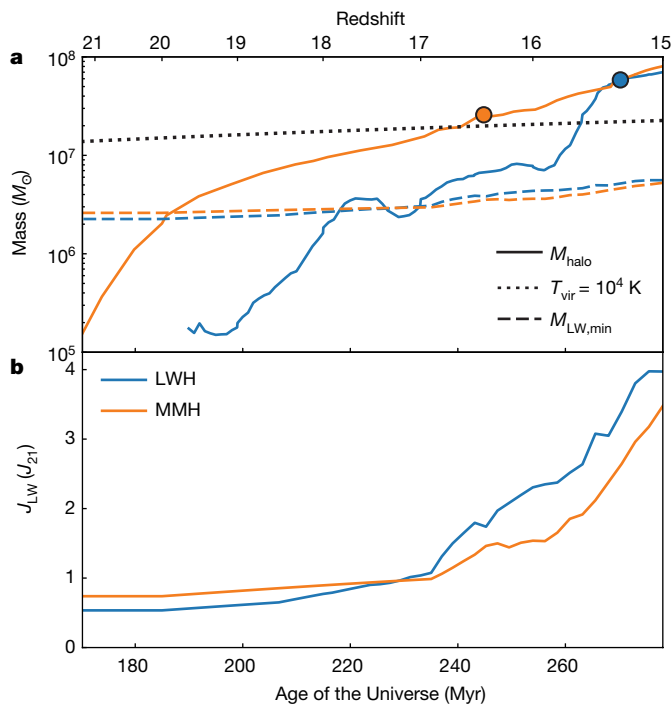


Fig. 2 | Mass growth histories of the target haloes. We show the evolution of the metal-free atomic-cooling haloes with the highest mass (MMH; orange) and the highest Lyman–Werner flux (LWH; blue). **a**, Halo mass (M_{halo} ; solid) compared with the minimum mass for H_2 cooling ($M_{\text{LW,min}}$; dashed) and the minimum mass for atomic cooling (corresponding to the mass of a halo with a virial temperature of $T_{\text{vir}} = 10^4$ K; dotted). The circles indicate when the haloes experience gravitational collapse into a massive black hole. The MMH grows smoothly and has a growth history that is more typical of an atomic-cooling halo. By contrast, the LWH undergoes rapid growth just before collapse, growing by a factor of six within 10 Myr. **b**, Lyman–Werner flux J_{LW} at the densest point of each halo in units of J_{21} . The flux is increasing from the nearby, growing group of young galaxies at a distance of 10–15 kpc.

Standard cold dark-matter cosmologies predict that large-scale structure forms hierarchically. Smaller objects that form at early times subsequently merge and grow into larger objects. The existence of supermassive black holes^{15,16} with masses of around $10^9 M_\odot$ (where M_\odot is the solar mass) only 800 Myr after the Big Bang indicates that there must have been an early intense convergence of mass in ‘rare’ locations, occurring only roughly ten times per co-moving cubic gigaparsec.

We performed cosmological radiation hydrodynamics simulations (Renaissance simulations; see Methods) using the code Enzo¹⁷ to elucidate the formation of the first generation of stars and galaxies in the Universe^{11,12}. The simulations include models for the formation of massive metal-free (population III) stars and subsequently of metal-enriched stars similar to those found in the Galaxy. We follow the effects of the ionizing radiation of these stars¹⁸ and of supernova explosions on their environments as galaxies first assemble, both of which are important in regulating early galaxy formation.

Motivated by the possible early formation of supermassive stars (SMSs), we analyse the region from the Renaissance simulation suite that is centred on the densest cosmological co-moving volume (133.6 Mpc^3), which contains 822 galaxies at its ending redshift of $z = 15$ (270 Myr after the Big Bang). We identify candidate SMS host haloes by searching the simulation for metal-free atomic-cooling haloes without prior star formation at $z = 15$. We place no constraints on the level of Lyman–Werner flux impacting the haloes. There are 670 atomic-cooling haloes, ten of which are metal-free and have not hosted prior star formation (Extended Data Table 1). The remaining atomic-cooling haloes have formed stars prompted by either H_2 or metal-line cooling and are not conducive to the formation of SMSs (and subsequently direct-collapse black holes, DCBHs). Out of these ten haloes, we concentrate on two—the most

massive halo (MMH) and the halo exposed to the most Lyman–Werner radiation flux (LWH). We resample the mass distributions of these two haloes at $z = 20$ and at a mass resolution higher by a factor of 169, and re-simulate them to study their gravitational collapse in more detail.

Both haloes assemble in a region 10–25 kpc away from a group of young galaxies that have photo-ionized, photo-heated and chemically enriched the surrounding environments (Fig. 1). At $z = 18$, the young galaxies near the MMH (Fig. 1a–d) have created an amorphous H II region with a maximum extent of 20 kpc. As the star-formation rates grow in these young (massive) galaxies, the Lyman–Werner intensities increase from $J_{\text{LW}} \approx 1J_{21}$ at $z = 18$ within 5 physical kpc of the galaxies to $J_{\text{LW}} \approx 30J_{21}$ at $z = 15$, where J_{21} is the intensity of the background radiation in units of $10^{-21} \text{ erg cm}^{-2} \text{ s}^{-1} \text{ Hz}^{-1} \text{ sr}^{-1}$. The only other source of Lyman–Werner radiation comes from four nearby haloes that host population III stars, 3–5 kpc from the LWH. Both target haloes are impacted by a Lyman–Werner intensity of $J_{\text{LW}} \approx 3J_{21}$ at $z = 15$ (Fig. 1d, h). This flux is 6 to 600 times lower than previous estimates for the critical Lyman–Werner flux necessary for SMS formation^{19–21}.

The metal-enriched regions around the group of young galaxies extend a distance of only 5 kpc, still far from the target haloes. The heavy elements in these regions originate from both population III progenitors and ongoing star formation in the galaxies. Over the next 60 Myr, the ionizing radiation from the young, growing galaxies near both target haloes will extend the H II regions to nearly 40 kpc in radius (Fig. 1). This will leave most of the intergalactic medium and associated collapsed haloes chemically pristine, but nonetheless bathed in Lyman–Werner radiation, which will help to prevent population III star formation.

During the process of halo assembly (Fig. 2a), the Lyman–Werner intensity increases from $0.3J_{21}$ to $3J_{21}$ at $z = 15$ (Fig. 2b), corresponding to a minimum halo mass of $M_{\text{crit}} \approx 3 \times 10^6 M_\odot$ that can support H_2 cooling²² and primordial star formation. However, the MMH (LWH) gravitationally collapses only after it reaches the atomic-cooling limit at $z = 16.4$ ($z = 15.3$), when it has a mass of $2.6 \times 10^7 M_\odot$ ($5.8 \times 10^7 M_\odot$)—an order of magnitude above M_{crit} . Upon closer inspection, we find that both target haloes experience a period of rapid growth in mass (Fig. 2a). The MMH grows by a factor of 30 over 30 Myr ($z = 21$ –19) as it virializes. The LWH experiences two rapid growth events. It first increases from $2 \times 10^5 M_\odot$ to $3 \times 10^6 M_\odot$ between $z = 19$ and $z = 18$ (15 Myr), at which point its mass fluctuates just above M_{crit} . Then at $z = 15.8$ it grows markedly, by a factor of nine within 10 Myr. Most of the accreted matter originates from the parent filament, a major merger and several minor halo mergers. This rapid convergence of matter below the atomic-cooling limit is a prediction of the standard cold dark-matter paradigm, and in conflict with cosmologies that suppress power below the atomic-cooling limit. Nevertheless, rapid convergence is rare, occurring in only about 0.03% of haloes (Methods) with similar masses and that exist in an large-scale overdense environment.

Gas within these growing haloes is dynamically heated as it evolves to virial equilibrium, with a heating rate that is linearly proportional to the mass growth rate of the halo¹³. Dynamical heating is important only when gas cooling is inefficient, particularly in rapidly growing low-mass haloes. In combination with Lyman–Werner negative feedback, it can further suppress gravitational collapse. Both target haloes sustain substantial dynamical heating during their rapid growth events, driven primarily by major mergers. We find that major mergers are the dominant mechanism for preventing population III star formation in these haloes.

The simulations follow the evolution of the target haloes until they reach a density of $10^{-15} \text{ g cm}^{-3}$, at which point it is certain that a collapsed object will form (Supplementary Videos 1 and 2). Both haloes form a gravitationally unstable core, which for the MMH (LWH) has a mass of $3 \times 10^4 M_\odot$ ($2 \times 10^5 M_\odot$) and a radius of 3 pc (15 pc). The MMH grows gradually after its rapid growth event, which allows the system to form a rotationally supported disk that is cold (300 K) compared to the surrounding gas (10,000 K). The medium within the cold disk is turbulent, which causes numerous weak shocks (Fig. 3d). The disk then fragments into three clumps (Fig. 3a, b), which all of which proceed to collapse because thermal pressure and rotational forces cannot counteract the

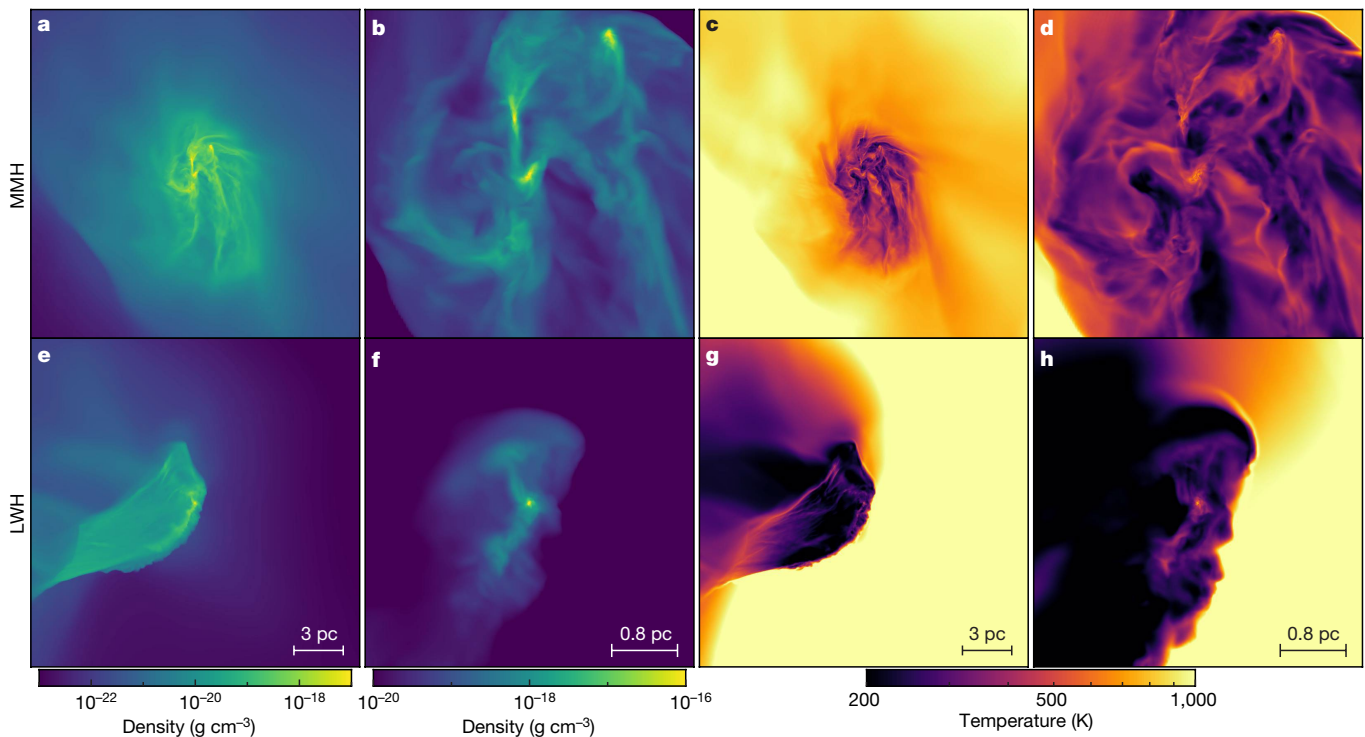


Fig. 3 | Morphology of the collapsing objects. **a–h**, Density-weighted projections of the gas density (**a**, **b**, **e**, **f**) and temperature (**c**, **d**, **g**, **h**) of the MMH (**a–d**) and the LWH (**e–h**) at the end of the simulations, centred on the densest point and aligned to be perpendicular to the angular momentum vector of the disk. The images in **b**, **d**, **f** and **h** are close-ups of those in **a**, **c**, **e** and **g**, respectively. The MMH forms a cold disk that

fragments into three clumps, accompanied by weak turbulent shocks within the disk. In the LWH, a dense and cold sheet forms after the collision of two progenitor haloes, where a single clump collapses after becoming self-gravitating. Within a radius of 0.1 pc in all of the clumps, adiabatic compression heats the gas.

gravitational forces of the clumps (Methods). The morphology of the LWH is completely different from that of the MMH because of a recent major merger. The collision causes a sheet-like overdensity (Fig. 3e) that cools to 300 K, becoming gravitationally unstable to fragmentation. A single clump fragments from the sheet (Fig. 3f) and undergoes catastrophic collapse. All clumps in both target haloes have masses of around $10^3 M_\odot$.

The radial profiles of the gas density (Fig. 4a) generally follow a power law with a slope of -2 , as expected for an isothermal collapse. The density can be integrated with respect to radius to obtain a radial mass coordinate that corresponds to the gas mass enclosed within a given radius (Fig. 4b). Deviations from a power law—seen as spikes

around 1 pc for the MMH and an inflection point around 1 pc for the LWH—originate from the two other clumps in the MMH and from the sheet-like structure in the LWH, respectively. The gas inside the Jeans mass (marked with squares in Fig. 4) becomes shielded from the extragalactic Lyman–Werner background, allowing the H_2 fraction to increase to 10^{-3} , which is sufficient to cool the gas to 300 K (Fig. 4c). Inside a radial mass coordinate of $10^3 M_\odot$, adiabatic compression heats the gaseous core to 600–800 K.

The key indicator for SMS formation is rapid gas inflow onto the gravitationally unstable core, not the overall Jeans mass. It has been shown that accretion rates of more than about $0.04 M_\odot \text{ yr}^{-1}$ onto a nascent, central core will result in SMS formation^{9,23}. The weak

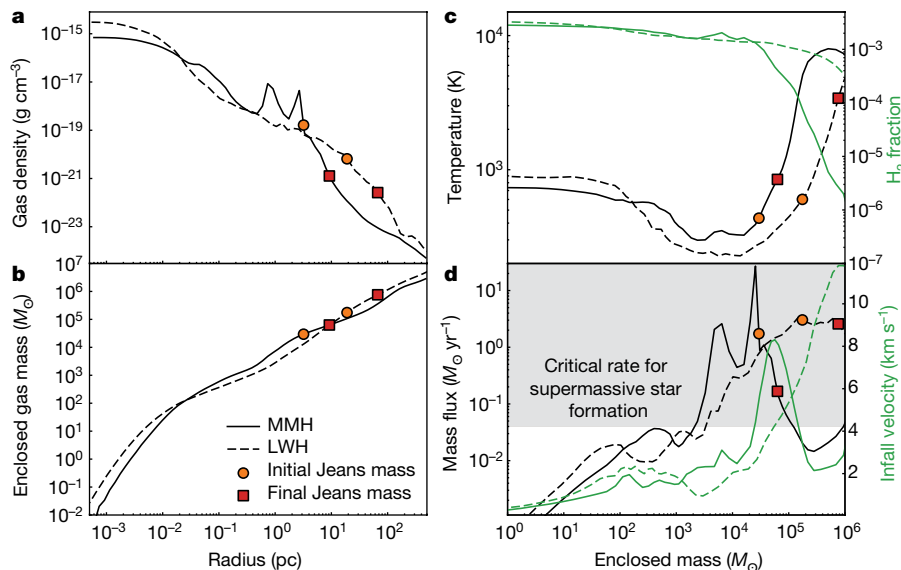


Fig. 4 | Gravitational collapse of the target haloes. **a–d**, Radially averaged profiles of gas density (**a**), enclosed gas mass (**b**), gas temperature (**c**; black lines), H_2 fraction (**c**; green lines), radial mass inflow rates (**d**; black lines) and radial infall velocities (**d**; green lines) in the MMH (solid) and the LWH (dashed). The orange circles indicate the Jeans mass at that mass scale when the objects first become gravitationally unstable; the red squares represent the same quantities at the end of the simulation. At the surface of the gravitationally unstable core, gas is infalling at rates of more than $0.1 M_\odot \text{ yr}^{-1}$; values above $0.04 M_\odot \text{ yr}^{-1}$ (grey shaded region in **d**) can induce and fuel the formation of supermassive stars.

hydrogen-ionizing luminosities of SMSs cannot reverse these strong gas flows^{24,25}. The respective infalling mass fluxes (Fig. 4d) at the Jeans mass at the final time are $0.17M_{\odot} \text{ yr}^{-1}$ and $2.1M_{\odot} \text{ yr}^{-1}$ for the MMH and the LWH, above the critical value for SMS formation. This ample supply of inflowing gas provides fuel for the clumps within the central unstable object. The infall rates onto the clumps (Extended Data Fig. 7a) are between $0.03M_{\odot} \text{ yr}^{-1}$ and $0.08M_{\odot} \text{ yr}^{-1}$ at the boundaries of the clumps, but increase rapidly to about $0.5M_{\odot} \text{ yr}^{-1}$ at a radial mass coordinate of 10^4M_{\odot} . This finding suggests that after the final snapshot of our simulation the cores continue to grow rapidly for 1 Myr, similar to the typical lifetime of a SMS (Extended Data Fig. 7b). We therefore conclude that within 1 Myr the two target haloes will host SMS formation and subsequently a DCBH with an initial seed mass of at least 10^3M_{\odot} , and perhaps up to 10^4M_{\odot} .

Using the formation requirements discussed above, we estimate (Methods) the formation rate of DCBHs per co-moving volume to be $1.1_{-0.91}^{+1.7} \times 10^{-3} \text{ Mpc}^{-3}$ (68% confidence interval) for each SMS that forms through this new formation scenario in overdense regions of the Universe. Given that overdense regions make up only 0.01%–0.1% of the Universe, the global number density of DCBH formation is predicted to be 10^{-7} – 10^{-6} Mpc^{-3} (co-moving), 100–1,000 times higher than previous estimates²⁶.

SMSs and therefore DCBHs that form in rapidly growing haloes, as proposed here, will be tens of kiloparsecs away from the large-scale overdensity. They will take hundreds of millions of years—a substantial fraction of the age of the Universe at $z > 6$ —to fall into the nearby group of galaxies. We predict that these DCBHs will evolve to form the population of faint quasars observed^{27,28} at $z \approx 6$. This population will be within the reach of the James Webb Space Telescope, which will be able to provide stringent constraints on their number densities that will be directly comparable to our results.

Online content

Any methods, additional references, Nature Research reporting summaries, source data, statements of data availability and associated accession codes are available at <https://doi.org/10.1038/s41586-019-0873-4>.

Received: 21 February 2018; Accepted: 30 November 2018;

Published online: 23 January 2019

- Volonteri, M. The formation and evolution of massive black holes. *Science* **337**, 544–547 (2012).
- Greif, T. H. The numerical frontier of the high-redshift Universe. *Comput. Astrophys. Cosmol.* **2**, 3 (2015).
- Omukai, K. Primordial star formation under far-ultraviolet radiation. *Astrophys. J.* **546**, 635–651 (2001).
- Begelman, M. C., Volonteri, M. & Rees, M. J. Formation of supermassive black holes by direct collapse in pre-galactic haloes. *Mon. Not. R. Astron. Soc.* **370**, 289–298 (2006).
- Hosokawa, T., Omukai, K. & Yorke, H. W. Rapidly accreting supergiant protostars: embryos of supermassive black holes? *Astrophys. J.* **756**, 93 (2012).
- Ardaneh, K. et al. Direct collapse to supermassive black hole seeds with radiation transfer: cosmological haloes. *Mon. Not. R. Astron. Soc.* **479**, 2277–2293 (2018).
- Habouzit, M., Volonteri, M., Latif, M., Dubois, Y. & Peirani, S. On the number density of ‘direct collapse’ black hole seeds. *Mon. Not. R. Astron. Soc.* **463**, 529–540 (2016).
- Chon, S., Hosokawa, T. & Yoshida, N. Radiation hydrodynamics simulations of the formation of direct-collapse supermassive stellar systems. *Mon. Not. R. Astron. Soc.* **475**, 4104–4121 (2018).
- Hosokawa, T., Yorke, H. W., Inayoshi, K., Omukai, K. & Yoshida, N. Formation of primordial supermassive stars by rapid mass accretion. *Astrophys. J.* **778**, 178 (2013).
- Umeda, H., Hosokawa, T., Omukai, K. & Yoshida, N. The final fates of accreting supermassive stars. *Astrophys. J.* **830**, L34 (2016).
- O’Shea, B. W., Wise, J. H., Xu, H. & Norman, M. L. Probing the ultraviolet luminosity function of the earliest galaxies with the renaissance simulations. *Astrophys. J.* **807**, L12 (2015).
- Xu, H., Wise, J. H., Norman, M. L., Ahn, K. & O’Shea, B. W. Galaxy properties and UV escape fractions during the epoch of reionization: results from the Renaissance simulations. *Astrophys. J.* **833**, 84 (2016).
- Yoshida, N., Abel, T., Hernquist, L. & Sugiyama, N. Simulations of early structure formation: primordial gas clouds. *Astrophys. J.* **592**, 645–663 (2003).
- Fernandez, R., Bryan, G. L., Haiman, Z. & Li, M. H₂ suppression with shocking inflows: testing a pathway for supermassive black hole formation. *Mon. Not. R. Astron. Soc.* **439**, 3798–3807 (2014).

- Mortlock, D. J. et al. A luminous quasar at a redshift of $z = 7.085$. *Nature* **474**, 616–619 (2011).
- Bañados, E. et al. An 800-million-solar-mass black hole in a significantly neutral Universe at a redshift of 7.5. *Nature* **553**, 473–476 (2018).
- Bryan, G. L. et al. ENZO: an adaptive mesh refinement code for astrophysics. *Astrophys. J. Suppl. Ser.* **211**, 19 (2014).
- Wise, J. H. & Abel, T. ENZO+MORAY: radiation hydrodynamics adaptive mesh refinement simulations with adaptive ray tracing. *Mon. Not. R. Astron. Soc.* **414**, 3458–3491 (2011).
- Shang, C., Bryan, G. L. & Haiman, Z. Supermassive black hole formation by direct collapse: keeping protogalactic gas H₂ free in dark matter haloes with virial temperatures $T_{\text{vir}} \gtrsim 10^4 \text{ K}$. *Mon. Not. R. Astron. Soc.* **402**, 1249–1262 (2010).
- Agarwal, B., Smith, B., Glover, S., Natarajan, P. & Khochfar, S. New constraints on direct collapse black hole formation in the early Universe. *Mon. Not. R. Astron. Soc.* **459**, 4209–4217 (2016).
- Glover, S. C. O. Simulating the formation of massive seed black holes in the early Universe – I. An improved chemical model. *Mon. Not. R. Astron. Soc.* **451**, 2082–2096 (2015).
- Machacek, M. E., Bryan, G. L. & Abel, T. Simulations of pregalactic structure formation with radiative feedback. *Astrophys. J.* **548**, 509–521 (2001).
- Schleicher, D. R. G., Palla, F., Ferrara, A., Galli, D. & Latif, M. Massive black hole factories: supermassive and quasi-star formation in primordial halos. *Astron. Astrophys.* **558**, A59 (2013).
- Hosokawa, T. et al. Formation of massive primordial stars: intermittent UV feedback with episodic mass accretion. *Astrophys. J.* **824**, 119 (2016).
- Sakurai, Y., Hosokawa, T., Yoshida, N. & Yorke, H. W. Formation of primordial supermassive stars by burst accretion. *Mon. Not. R. Astron. Soc.* **452**, 755–764 (2015).
- Hirano, S., Hosokawa, T., Yoshida, N. & Kuiper, R. Supersonic gas streams enhance the formation of massive black holes in the early universe. *Science* **357**, 1375–1378 (2017).
- Onoue, M. et al. Minor contribution of quasars to ionizing photon budget at $z \sim 6$: update on quasar luminosity function at the faint end with Subaru/Suprime-Cam. *Astrophys. J.* **847**, L15 (2017).
- Kim, Y. et al. The Infrared Medium-deep Survey. IV. The low Eddington ratio of a faint quasar at $z \sim 6$: not every supermassive black hole is growing fast in the early Universe. *Astrophys. J.* **855**, 138 (2018).
- Turk, M. J. et al. yt: a multi-code analysis toolkit for astrophysical simulation data. *Astrophys. J. Suppl. Ser.* **192**, 9 (2011).

Acknowledgements J.H.W. thanks A. Benson for assistance with the code Galacticus. J.H.W. was supported by NSF awards AST-1614333 and OAC-1835213, NASA grant NNX17AG23G, and Hubble theory grant HST-AR-14326. J.A.R. acknowledges support from the EU commission via the Marie Skłodowska-Curie Grant ‘SMARTSTARS’ (grant number 699941). B.W.O. was supported in part by NSF awards PHY-1430152, AST-1514700 and OAC-1835213, by NASA grants NNX12AC98G and NNX15AP39G, and by Hubble theory grants HST-AR-13261.01-A and HST-AR-14315.001-A. M.L.N. was supported by NSF grants AST-1109243, AST-1615858 and OAC-1835213. The simulation was performed on Blue Waters operated by the National Center for Supercomputing Applications (NCSA) with PRAC allocation support by the NSF (awards ACI-0832662, ACI-1238993 and ACI-1514580). The subsequent analysis and the re-simulations were performed with NSF’s XSEDE allocation AST-120046 on the Stampede2 resource. This research is part of the Blue Waters sustained-petascale computing project, which is supported by the NSF (awards OCI-0725070 and ACI-1238993) and the state of Illinois. Blue Waters is a joint effort of the University of Illinois at Urbana-Champaign and its NCSA. The freely available astrophysical analysis code yt²⁹ and plotting library matplotlib were used to construct numerous plots within this paper. Computations described in this work were performed using the publicly available Enzo code, which is the product of a collaborative effort of many independent scientists from numerous institutions.

Reviewer information Nature thanks N. Yoshida and the other anonymous reviewer(s) for their contribution to the peer review of this work.

Author contributions J.H.W. and J.A.R. conceived the idea, performed the analysis and drafted the paper. The Renaissance simulations were conducted by H.X. and J.H.W., and the re-simulations of the target haloes were conducted by J.H.W. B.W.O. performed the Monte Carlo analysis for the number density estimate. All authors contributed to the interpretation of the results and to the text of the final manuscript.

Competing interests The authors declare no competing interests.

Additional information

Extended data is available for this paper at <https://doi.org/10.1038/s41586-019-0873-4>.

Supplementary information is available for this paper at <https://doi.org/10.1038/s41586-019-0873-4>.

Reprints and permissions information is available at <http://www.nature.com/reprints>.

Correspondence and requests for materials should be addressed to J.H.W.

Publisher’s note: Springer Nature remains neutral with regard to jurisdictional claims in published maps and institutional affiliations.

METHODS

Cosmological simulation of early galaxy formation. The Renaissance simulations were carried out using the open-source adaptive mesh-refinement code Enzo¹⁷—a physics-rich, highly adaptive code that has been tuned for high-redshift structure-formation simulations^{11,30–32}. The Renaissance simulations have been detailed previously^{11,12,33–37}; here we summarize the simulation characteristics relevant to this study. All of the Renaissance simulations were carried out in a co-moving volume of 40 Mpc × 40 Mpc × 40 Mpc. We set the cosmological parameters using the 7-year WMAP Λ CDM+SZ+LENS best fit³⁸: $\Omega_m = 0.266$, $\Omega_\Lambda = 0.734$, $\Omega_b = 0.0449$, $h = 0.71$, $\sigma_8 = 0.81$ and $n = 0.963$. Here h is the Hubble parameter in units of 100 km s^{−1} Mpc^{−1}; Ω_Λ , Ω_m and Ω_b are the fractions of critical energy density of vacuum energy, total matter and baryons, respectively; σ_8 is the root-mean-square density fluctuation inside a sphere of radius 8/h Mpc; and n is the slope of the primordial scalar power spectrum. The simulations were initially run until a redshift of $z = 6$ at relatively coarse resolution with 512³ particles, each with a mass of $1.7 \times 10^7 M_\odot$. Three regions of interest were then selected for re-simulation with much higher refinement: a rare-peak region, a normal region and a void region. The rare-peak region has a co-moving volume of 133.6 Mpc³, whereas the normal and void regions each have co-moving volumes of 220.5 Mpc³.

In this study, we focus on the rare-peak simulation, which was selected by extracting the Lagrangian region centred on two $3 \times 10^{10} M_\odot$ haloes at $z = 6$, the most massive at that time. The dimensions of the rare-peak region were set at 5.2 Mpc × 7.0 Mpc × 8.3 Mpc. The simulation was re-initialized using MUSIC³⁹, with a further three nested grids centred on the rare-peak region. This led to an effective resolution of 4,096³ and a dark-matter particle resolution of $2.9 \times 10^4 M_\odot$ within the region of highest refinement. During the course of the simulation, further adaptive refinement is allowed within the refinement zone (the Lagrangian region of the rare-peak) up to a maximum level of 12, leading to a maximum spatial resolution of 19 co-moving pc (1.2 proper pc at $z = 15$). The simulation was halted at a final redshift $z = 15$ owing to the high computational expense. The mass function of the halo is well resolved down to $2 \times 10^6 M_\odot$, with 70 particles per halo¹², and at the final redshift the simulations contained 822 galaxies with at least 1,000 particles ($M_{\text{halo}} \approx 2.9 \times 10^7 M_\odot$). We follow the ionization states of hydrogen and helium with a nine-species primordial non-equilibrium chemistry and cooling network⁴⁰, supplemented by metal-dependent cooling tables⁴¹. Dark-matter halo catalogues and the associated merger trees were created with Rockstar⁴² and consistent-trees⁴³, respectively.

Star formation and feedback. The Renaissance simulations include both self-consistent population III and metal-enriched star formation at the maximum refinement level. The simulation captures star formation in haloes as small as $3 \times 10^6 M_\odot$. Population III star formation occurs when a cell meets all of the following criteria: (1) an overdensity with respect to the mean density of the Universe of 5×10^5 (about 10^3 cm^{-3} at $z = 10$); (2) converging gas flow ($\nabla \cdot \mathbf{v}_{\text{gas}} < 0$); and (3) a molecular hydrogen fraction of $f_{\text{H}_2} > 5 \times 10^{-4}$.

These physical conditions are typical of collapsing metal-free molecular clouds about 10 Myr before the birth of a population III main-sequence star³⁰. In this scenario, each star particle within the simulation represents a single star. Population III star formation occurs if the metallicity is less than 10^{-4} of the solar fraction in the highest-density cell, with metal-enriched star formation proceeding otherwise. Population III star formation further requires that $f_{\text{H}_2} > 5 \times 10^{-4}$. This takes into account the fact that star formation should not proceed in the presence of a strong Lyman–Werner (LW) radiation field. The functional form of the initial mass function (IMF) and supernovae feedback are calibrated⁴⁴ against high-resolution population III star-formation simulations, stellar evolution models, and observations and models of star formation in local molecular clouds. Stellar feedback uses the Moray radiative transport framework¹⁸ for ionizing photons. LW radiation that dissociates H₂ is modelled using an optically thin, inverse-square profile, centred on all star particles. We do not include any H₂ self-shielding, which is important only at high densities. In particular, DCBH host halo candidates shield themselves from a background only at scales⁴⁵ below 3 pc, which is close to our resolution limit. A LW background radiation field is also included to model radiation from stars outside the simulation volume⁴⁴ that is added to the spatially varying LW radiation field created by stars inside the volume. In the high-density region of the rare-peak simulation, the LW radiation from stars dominates the background. Although we cannot follow population III star formation in haloes below $3 \times 10^6 M_\odot$, it is suppressed by the LW background in such haloes^{22,46,47} and by baryonic streaming velocities in certain regions^{26,48}. Therefore, we are confident that our simulation follows the complete star-formation history of all collapsed structure, and thus the metal-enrichment history of pre-galactic gas that is vital to determining the conditions for DCBH formation.

Direct-collapse black holes. The star formation and feedback models do not include a DCBH formation model but consider the appropriate astrophysical processes to ascertain the chemical and thermal state of all collapsed objects resolved by the simulation, essential for searching for candidate DCBH formation sites.

Also critical to any DCBH formation scenario is the inclusion of population III star formation and its supernova feedback that generally enriches typical pre-galactic material with heavy elements. The emergence of a DCBH/SMS environment is therefore a robust prediction of the Renaissance simulations. The dark-matter resolution in the original Renaissance simulations is not sufficient to follow the detailed collapse of these objects⁴⁹; however, the re-simulations (see next section) of the target haloes have an ultimate mass and spatial resolution of $103 M_\odot$ and 60 AU, allowing us to accurately follow the dynamics of the collapsing halo and determine whether its gas infall rate is large enough to support SMS and thus DCBH formation.

High-resolution simulations of target haloes. After identifying the candidate haloes in the Renaissance simulations, we re-simulate the two target haloes at higher mass and spatial resolution, starting at $z = 20$. We first identify the dark-matter particles within three virial radii of the target haloes at the final redshift, $z = 15$. Using their unique particle identifiers, we determine their positions at $z = 20$ and split their mass equally into 13 particles. Twelve of the child particles are placed at the 12 vertices of a hexagonal close-packed array, and the remaining particle is placed at the original particle position⁵⁰. We recursively split the particles twice, decreasing the dark-matter particle mass by a factor of 13^2 to $103 M_\odot$ in the Lagrangian region of the target haloes. This method of particle splitting is widely used in high-resolution cosmological simulations^{49,51–53}; however, it may induce artificial smoothing of the density field⁵⁴ and does not add additional small-scale power to the matter distribution.

The Renaissance simulations show that the target haloes remain metal-free and are not exposed to any ionizing radiation. Their thermodynamic evolution and collapse are therefore primarily controlled by the growth history of the halo and the impinging LW flux. With these priors, we can safely neglect star formation and feedback, focusing on the dynamics of collapse. We impose a uniform LW radiation background that is time-dependent and is taken from the flux measured at the centre of the most massive progenitor halo in the original simulation (see Fig. 2b). Spatial deviations from this value are less than a few per cent within the Lagrangian region and do not affect the thermodynamics of the gas.

In addition to the increased mass resolution, we increase the spatial resolution by resolving the local Jeans length by at least 16 cells, whereas the original simulation did not have enough mass resolution to enforce such a refinement criterion. We use this initial re-simulation to identify the time of collapse. We then restart the simulations a free-fall time (approximately 20 Myr) before the collapse time, further increasing the spatial resolution so that the Jeans length is resolved by at least 64 cells. Computational limitations restrict us from running at such high resolution for the entirety of the re-simulation; therefore, we increase the resolution only during the final stages of the collapse. We also include H₂ self-shielding of the LW radiation field during this final re-simulation⁵⁵ and compute the primordial cooling rates with the software library Grackle⁵⁶. We enforce a maximum refinement level of 24, corresponding to a co-moving (physical at $z = 15$) resolution of 960 AU (60 AU). We stop the re-simulations once they reach this maximum refinement level. We smooth the dark-matter density field at scales below 9.5 co-moving pc (0.6 physical pc at $z = 15$; refinement level 13). At these scales, the gas density dominates the matter density, and by smoothing the dark-matter density we remove any artefacts associated with the discrete representation of the dark-matter mass distribution³⁰.

Dynamical heating. For a halo to potentially host a SMS or DCBH, it must grow to the atomic-cooling limit without forming stars or being chemically enriched; any efficient cooling must therefore be suppressed. LW radiation can suppress H₂ formation and dynamical heating can counteract any H₂ cooling in low-mass haloes. The dynamical heating rate¹³ is

$$\Gamma_{\text{dyn}} = \alpha M_{\text{halo}}^{-1/3} \frac{k_B}{\gamma - 1} \frac{dM_{\text{halo}}}{dt}$$

where α is a coefficient⁵⁷ relating the virial mass and temperature of the halo ($T_{\text{halo}} = \alpha M_{\text{halo}}^{2/3}$), M_{halo} is the total halo mass, k_B is the Boltzmann constant and $\gamma = 5/3$ is the adiabatic index. This process is relevant only when the radiative cooling rates $\Lambda(T_{\text{halo}})$ per hydrogen atom have similar values. Below the atomic-cooling limit, chemically primordial haloes rely on the inefficient coolant H₂ to collapse and form stars. Radiative cooling will thus be suppressed when $\Gamma_{\text{dyn}} > n\Lambda$, where n is the hydrogen number density. This inequality sets a critical halo growth rate¹³

$$\left(\frac{dM_{\text{halo}}}{dt} \right)_{\text{crit}} = \frac{2\alpha}{3} \frac{\gamma - 1}{k_B} M_{\text{halo}}^{-1/3} n \Lambda(T_{\text{halo}}) \quad (1)$$

above which cooling is suppressed. Extended Data Fig. 1 compares the critical growth rates (coloured lines) for three different H₂ fractions, using equation (1), and the growth rates of the two target haloes (circles and triangles). We calculate the primordial cooling rate $\Lambda(T)$ for each H₂ fraction with Grackle⁵⁶. Typical

f_{H2} values in the centres of the target haloes before collapse are between 10^{-5} and 10^{-6} .

Absent of any dynamical heating, haloes can cool and collapse through H_2 once they reach a critical mass^{22,47}:

$$\frac{M_{\text{min,LW}}}{M_{\odot}} = 1.25 \times 10^5 + 2.65 \times 10^5 \left(\frac{J_{\text{LW}}}{J_{21}} \right)^{0.47}$$

shown as the dashed vertical line for $J_{\text{LW}} = 1J_{21}$, the intensity at both target haloes when they have such a mass. Atomic-hydrogen cooling becomes dominant over molecular cooling at $T \approx 7,000$ K (corresponding to a halo mass of $6 \times 10^6 M_{\odot}$ at $z = 15$; indicated by the sharp rise in the critical curves), above which dynamical heating becomes unimportant in the target haloes. In any chemically pristine halo unaffected by ionizing radiation, gravitational collapse ensues above this mass within a free-fall timescale. Models of SMS formation require infall rates above about $0.04 M_{\odot} \text{ yr}^{-1}$ that are driven only by deep gravitational potentials of atomic-cooling haloes, the mass of which are shown as the dotted vertical line at $2.2 \times 10^7 M_{\odot} [(1+z)/16]^{-3/2}$.

The MMH and LWH both assemble rapidly as they virialize, initially growing at a rate per unit redshift of $-dM/dz = (1-3) \times 10^6 M_{\odot}$ when they have a mass $M \leq 10^6 M_{\odot}$. Although H_2 formation is photo-suppressed at these low masses, dynamical heating is present in these early rapid periods of growth and have lasting effects on the halo gas. The infalling gas shocks near the halo centre, heating the halo to the virial temperature. Only after a sound-crossing time does the halo come into virial equilibrium. This takes 30 Myr for a $3 \times 10^6 M_{\odot}$ halo (150 pc radius) and a sound speed of 10 km s^{-1} .

As the haloes equilibrate they continue to grow, at a reduced rate but still above the critical $f_{\text{H2}} = 10^{-6}$ curve until a mass of $6 \times 10^6 M_{\odot}$. The MMH accretes at a nearly constant rate per unit redshift of $3 \times 10^6 M_{\odot}$, with a peak rate per unit redshift of $7 \times 10^6 M_{\odot}$ at $2 \times 10^6 M_{\odot}$. The growth rate per unit redshift of the LWH fluctuates between $10^6 M_{\odot}$ and $10^7 M_{\odot}$. When atomic cooling becomes efficient, catastrophic collapse occurs within a free-fall time $t_{\text{ff}} = \sqrt{3\pi/(32G\rho)}$ (where G is the gravitational constant) that is equal to 20 Myr for a density of $\rho = 10^{-23} \text{ g cm}^{-3}$, typical of haloes that are compressed adiabatically⁵⁸.

As shown in Fig. 2, the MMH undergoes one rapid growth event, starting at $2 \times 10^5 M_{\odot}$ at $z = 21$ as it virializes and occurring before H_2 cooling becomes efficient (and hence before the local LW flux becomes important). The rapid infall creates a shock near its centre, heating the halo gas over a sound-crossing time of 30 Myr. The halo gas stabilizes after this event and then collapses on a free-fall timescale of $t_{\text{ff}} \approx 20$ Myr, where $\rho \approx 10^{-23} \text{ g cm}^{-3}$ is the maximum gas density before collapse. After the rapid growth halts, the halo must grow to the atomic-cooling limit within 50 Myr, the sum of the sound-crossing and free-fall times. Otherwise, it will collapse when atomic cooling is not efficient, and it will cool through H_2 and fragment into more typical population III star formation. It collapses at $z = 16.4$ when its mass is just above the atomic-cooling limit. There are 75 Myr between these two redshifts, leaving 25 Myr for early rapid growth. Given that halo masses increase exponentially⁵⁹ ($dM/dz \propto \alpha M$ so $M(z) \propto e^{\alpha z}$), we can estimate a critical growth rate in those first 25 Myr (left thick grey line in Extended Data Fig. 1) using the mass difference between $z = 21$ and $z = 19.2$ (25 Myr), when it grows to $3 \times 10^6 M_{\odot}$. The LWH experiences two rapid growth episodes, the first of which is similar to that of the MMH. Afterwards, its mass hovers just above the critical value M_{crit} for efficient H_2 cooling. The later growth spurt occurs just before it starts to cool atomically, as seen by the increase in $-dM/dz$ to greater than $3 \times 10^7 M_{\odot}$. The associated dynamical heating delays the collapse of the LWH until its mass is $5.8 \times 10^7 M_{\odot}$, twice the atomic-cooling limit.

In general, for dynamical heating to suppress metal-free star formation, halo growth must be rapid from the H_2 -cooling limit to the atomic-cooling limit. More specifically, it must happen faster than a free-fall time (20 Myr). This sets another, more general, critical growth rate between these two halo mass regions, using the same approach as before. This rate is shown as the thick grey line in Extended Data Fig. 1 between the green $f_{\text{H2}} = 10^{-6}$ critical curve and the atomic-cooling limit. Any halo that grows faster than this rate will have its gravitational potential deepen faster than it can collapse, making it more likely to support strong radial inflows, conducive for SMS formation.

Gravitational collapse of the central core. After reaching the atomic-cooling threshold, the gas begins to cool rapidly and (dynamical) heating mechanisms are suppressed. Above a temperature of approximately 8,000 K, radiative cooling of neutral hydrogen sets an upper limit for the temperature of the halo inside the virial radius, inducing a rapid increase in density and ultimately gravitational collapse. Extended Data Fig. 2 shows the ratio of the enclosed mass and the Jeans mass (M_{enc}/M_J) against the enclosed gas mass. For gravitational collapse to take hold, the gas inside the collapsing core must exceed the Jeans mass of the gas. In Extended Data Fig. 2, any lines entering the shaded region are unstable to gravitational collapse. For the MMH, the core of the halo first becomes unstable with

an enclosed mass approximately $3 \times 10^4 M_{\odot}$ (orange circle). As the halo grows in mass, the region grows to almost $10^5 M_{\odot}$ by the end of the simulation, which is gravitationally unstable and in principal also subject to fragmentation. The LWH first crosses into a region of instability with an enclosed mass of greater than $10^5 M_{\odot}$, and by the end of the simulation the central region of almost $10^6 M_{\odot}$ has become unstable to gravitational collapse.

Support within the collapsing core. As the core regions of both haloes start to undergo gravitational collapse, as outlined above, thermal, turbulent and rotational support will act to counteract the gravitational collapse. If there is sufficient gas support, the gravitational collapse can be suppressed even though the Jeans mass has been exceeded. Extended Data Fig. 3 shows the thermal and turbulent sound speeds as functions of enclosed mass. The thermal sound speed c_s is calculated as

$$c_s = \sqrt{\frac{\gamma k_B T}{\mu m_H}}$$

where γ is the adiabatic index, k_B is the Boltzmann constant, T is the temperature, μ is the mean molecular weight and m_H is the hydrogen mass. In calculating the total pressure support of the gas, the impact of the turbulent velocity field must also be considered. We calculate the root-mean-square turbulent velocities of the gas by subtracting the bulk gas velocity from the velocity field. We compute the bulk velocity as the velocity of the native computational cells averaged over a spherical 32^3 grid that has cell widths much coarser than the simulation data. This grid has an outer radius equal to the virial radius, equally spaced angular bins and equally logarithmically spaced radial bins. We then approximate the bulk velocity of each native cell with the value of the spherical grid cell that contains the native cell centre.

The turbulent and thermal components act together to support the gas against collapse and create an effective sound speed, $c_{\text{eff}}^2 = c_s^2 + v_{\text{rms}}^2$. In Extended Data Fig. 3, we see that the infall speed always exceeds the effective sound speed at some enclosed mass, indicating that, at this scale, the thermal and turbulent support cannot support the gas against gravitational collapse. For the MMH, the infall speed exceeds the effective sound speed at approximately $10^5 M_{\odot}$. This is similar to the scale at which the gas also becomes Jeans-unstable, and so we define the radius of the collapsing core to be equal to this scale. For the LWH, the gas provides little or no thermal or turbulent support, and the gas is free to collapse on approximately the free-fall timescale.

Interestingly, in both cases, the radial inflow becomes transonic at scales between $10^3 M_{\odot}$ and $10^4 M_{\odot}$. This indicates that at mass scales greater than approximately $10^3 M_{\odot}$ any fragments are thermally and/or turbulently supported, and we do not expect fragmentation of the gas cloud below this scale. Any protostars forming within these clouds would have most of the gas contained in the fragment available for accretion. We examine more closely the possible fragmentation of the outer core into gas clouds in the next section.

Extended Data Fig. 4 shows the rotational support provided by the gas against gravitational collapse. The rotational velocity of the gas is calculated as $|j|/a_1$, the ratio of the specific angular momentum $|j|$ of the gas and the largest eigenvalue a_1 of the inertia tensor, corresponding to the largest axis of the system⁶⁰. The centre of these profiles are taken to be the maximum gas density, consistent with the rest of our analysis. We compare this rotational velocity against the Keplerian velocity $v_{\text{Kep}} = \sqrt{GM/r}$. The regions where the rotational velocity exceeds the Keplerian velocity are shaded and indicate regions of rotational support. The rotationally supported region in the MMH extends from $2 \times 10^3 M_{\odot}$ to $3.3 \times 10^5 M_{\odot}$. For the LWH, the region of rotational support is much smaller, spanning only from $7 \times 10^3 M_{\odot}$ to $6 \times 10^4 M_{\odot}$. The rotational velocities within $100 M_{\odot}$ are not well defined because the separation between the densest gas parcel and the rotation centre becomes comparable to the radius (0.02 pc) enclosing $100 M_{\odot}$. We therefore do not consider them to be rotationally supported from this analysis. The (disk-like) regions of rotational support are nonetheless unstable to fragmentation, and fragmentation of the disk does occur in the MMH.

Fragmentation of the collapsing core into gas clouds. As the cloud collapses, cooling instabilities can cause the gas to fragment into self-gravitating clumps. Such fragmentation can be stabilized by thermal pressure or centrifugal forces that can be quantified by the Toomre parameter:

$$Q = \frac{c_s \kappa}{\pi G \Sigma}$$

The system is stable if $Q > 1$. Here Σ is the gas surface density, and the epicyclic frequency κ is calculated directly from the data as

$$\kappa^2 = \frac{2\Omega}{r} \frac{d(r^2 \Omega)}{dr}$$

where $\Omega = v_{\text{rot}}/r$ is the angular velocity and r is the radius in cylindrical coordinates, with the z axis aligned with the total angular momentum vector of the Jeans-unstable

gas cloud. These expressions assume an axisymmetric object. However, the collapsed objects in both haloes have non-ideal geometries. It is therefore beneficial to consider a local measure of stability²⁶

$$Q_{\text{local}} \approx \frac{\Omega^2}{\pi G \rho} \quad (2)$$

that can identify unstable regions with arbitrary geometries. Extended Data Fig. 5 shows Q_{local} for both haloes in fields of view of 20 pc and 4 pc. In the MMH, the disk-like object is marginally stable in the spiral overdensities (Extended Data Fig. 5a). Within these arms, there are three clumps that have fragmented (Extended Data Fig. 5b) and started to collapse. In the LWH, the overdense sheet-like object, which is induced by a major merger, is unstable to fragmentation in many regions and marginally stable in the remainder of the object. However, their collapse times are spread out, resulting in only one (the first) clump to fragment out of the overdense sheet by the end of the simulation.

Extended Data Fig. 6a shows Q as a function of r , where we have aligned the cylindrical z axis with the total angular momentum vector of the inner 10 pc. We compare Q with the effective Q (Q_{eff}), where we substitute c_s by c_{eff} to include any turbulent-pressure support in the stability analysis. When considering only rotational support as a counterbalance to gravitational collapse, the MMH and LWH are unstable ($Q < 1$) within a radius of 3 pc and 8 pc, respectively. As we have shown, turbulent pressures are comparable to thermal pressures, and this additional support stabilizes the rotating system against fragmentation ($Q_{\text{eff}} > 1$) outside 0.8 pc and 0.1 pc in the MMH and LWH, respectively. The LWH is also susceptible to fragmentation at radii of 0.8 pc and 2 pc, where Q_{eff} becomes slightly less than unity.

From the dispersion relation

$$w_g^2 = \kappa^2 + k^2 v_{\text{rot}}^2 - 2\pi G k \Sigma$$

that is used to calculate the growth perturbations in a gaseous disk, the associated maximum growth rate⁶¹ of a perturbation, which occurs at $k_{\text{max}} = \kappa/c_{\text{eff}}Q_{\text{eff}}$, is

$$|w_{\text{max}}| = \frac{\kappa(1 + Q_{\text{eff}}^2)^{1/2}}{Q_{\text{eff}}}$$

Here k is the wavenumber and w_g is the growth rate. We define the growth time $t_{\text{grow}} = 1/w_{\text{max}}$ where $Q_{\text{eff}} < 1$ (Extended Data Fig. 6b). For such a perturbation to form before the system collapses, the growth time must be smaller than a free-fall time (Extended Data Fig. 6c), $t_{\text{grow}}/t_{\text{ff}} < 1$. For the MMH, this condition is valid for radii less than 0.03 pc, corresponding to $100M_{\odot}$ of enclosed gas mass. Between this radius and 1 pc, the system is unstable to fragmentation, but it is collapsing faster than it can fragment. This analysis is centred on the densest point, contained in one of the clumps. This indicates that any fragmentation at small scales will be surrounded by a monolithic rapid collapse, most probably suppressing further fragmentation as this matter falls inward. The two other clumps in the MMH form about 1 pc away. Because we compute these quantities within cylindrical shells, the clumps with small Q_{local} (see Extended Data Fig. 5) are averaged out. Once they fragment, they begin to gravitationally collapse. In the LWH, fragmentation can occur before collapse inside a radius of 0.1 pc. Here a single clump fragments from the sheet-like overdensity, produced by a recent major merger, with a radius of about 1 pc, which collapses faster than it can fragment at this length scale. This analysis shows that turbulence has a role in providing additional stabilization against fragmentation. The suppression of fragmentation allows for only a few clumps, at most, to form in the collapsing system before the most dense clump collapses on the free-fall timescale, $t_{\text{ff}} \approx 5,000$ yr. This behaviour allows for the rapid infall to be concentrated on these few clumps, strengthening the case for SMS formation.

Given that the system is unstable to fragmentation, we search for self-gravitating clouds using the clump finder provided with the analysis toolkit *yt*²⁹. We search for clumps that are gravitationally bound and have a minimum of 20 cells, where clumps are defined as topologically connected sets of cells and form a hierarchical set of objects. Because the LWH has only one clump that contains the densest point, we perform this analysis on only the MMH. We identify three clumps that are also visible in the density projections (Fig. 3b). Below we define t as the time before collapse, where $t = 0$ is a free-fall time after the final simulation output of the maximum density. The three clumps are orbiting in the disk, located 1–2 pc from the rotational centre, where there is no local density maximum.

Clump 1 contains the densest point in the simulation, and the projections (Fig. 3; Extended Data Fig. 5) and global radial profiles (Fig. 4; Extended Data Fig. 2–4, 6) are centred on it. Its mass initially fluctuates between $200M_{\odot}$ and $600M_{\odot}$ at $t = 30$ – 70 kyr as the two progenitor clumps orbit each other, changing between being topologically connected and disconnected in the process. Their separation decays as energy is dissipated during their close encounters, eventually

merging into a single clump at $t = 25$ kyr. It grows to a mass of $790M_{\odot}$ and is located 1.2 pc from the rotational centre at the final time.

Clump 2 is an elongated object that grows steadily in mass from $200M_{\odot}$ to $840M_{\odot}$, orbiting at a distance of 1.8 pc, located above clump 1 in the projections.

Clump 3 initially has a mass of $770M_{\odot}$, orbiting at a distance of 2.2 pc, located in the upper-right of the projections. At $t = 50$ kyr, it merges with another clump, increasing its mass from $950M_{\odot}$ to $1,400M_{\odot}$. The change in its distance from the rotation centre is associated with the change in its centre of mass after the merger. It grows very little afterwards, to a final mass of $1,500M_{\odot}$, while it migrates outward from 1.6 pc to 1.9 pc.

As the clumps evolve, they do not migrate inwards towards the disk centre, suggesting that mergers are not imminent between these three clumps. This strengthens the argument for three separate sites of SMS formation and potentially DCBH formation. Such systems may be detectable in the future through gravitational waves⁶².

Collapse characteristics of the fragments. We now examine the accretion rates and thermal support of the clumps that form in both the MMH and the LWH. In Extended Data Fig. 7a, we plot the infall rate of the gas versus the enclosed mass for each of the clumps (three for the MMH and one for the LWH). The infall rates are computed as the mass flux through spherical shells and show a steady and near monotonic increase in infall rate as a function of enclosed mass. The infall rate for the LWH is more than a factor of three greater than that for the three major clumps identified within the MMH. This is probably due to the increased mass, at collapse time, and the higher radial velocity associated with the LWH. The LWH experiences a major merger less than 10 Myr before the end of the simulation that drives gas towards the centre, thus explaining the increased infall rates.

Circles in Extended Data Fig. 7a mark the infall rate at the clump mass. This is the infall rate that the outer part of the gas clump experiences. The rates onto each clump are very similar, with values between $0.01M_{\odot} \text{ yr}^{-1}$ and $0.1M_{\odot} \text{ yr}^{-1}$. These values are consistent with those obtained for a singular isothermal sphere collapse⁶³. However, this is the infall rate onto the outer gas clump and must be treated as an upper limit when ascribing it to the accretion rate onto a protostar that may subsequently form within the gas clump. Nonetheless, the infall rates are very high and sufficient to drive a protostar towards SMS formation.

In Extended Data Fig. 7b we plot the infall time against enclosed mass, which is calculated as the ratio of the mass enclosed and infall rate. The infall time can be used to compare against star formation timescales directly. Within an enclosed mass of $100M_{\odot}$, the timescale for each clump is approximately 10 kyr. The Kelvin–Helmholtz timescale for massive stars (up to about $100M_{\odot}$) is less than 100 kyr. The stars that form within these gas clumps will therefore reach the main sequence while still accreting, as is the case for SMS formation. Given the timescales shown here, the infall rates suggest that the (super)massive protostars will reach masses of at least $100M_{\odot}$ before reaching the main sequence⁶⁴. If the accretion onto the clump continues to remain rapid at that point, full gravitational contraction will be avoided (so-called ‘hot accretion’ flows) and the stellar envelope will remain bloated, leading to SMS formation in this context^{5,9,65,66}. After its formation, SMS lifetimes are around 1 Myr, suggesting that the whole gas cloud could be accreted before the star exhausts its hydrogen supply. SMSs with accretion rates below $0.1M_{\odot} \text{ yr}^{-1}$ experience a general relativistic instability, creating a massive black hole with a mass similar to that of its progenitor, when its nuclear fuel is exhausted. For higher accretion rates, the collapse occurs when the star is still burning hydrogen or helium¹⁰, producing black holes with masses between $2 \times 10^5 M_{\odot}$ and $8 \times 10^5 M_{\odot}$. Lastly, there is a peculiar case when the SMS has a mass of around $5.5 \times 10^4 M_{\odot}$ that produces an extremely energetic supernova⁶⁷.

In Extended Data Fig. 8, we plot the fractional support against collapse, similarly to Extended Data Fig. 3. We do this by again comparing the thermal, turbulent and infall velocities of the clumps. Extended Data Fig. 8a shows the velocities of the clump found for the LWH. Extended Data Fig. 8b–d shows the clump velocities of each of the three clumps found for the MMH. We find that in all cases the clumps are thermally supported and stable against further gravitational collapse. The radial inflows are subsonic for all four clumps, although the clump in the LWH contains transonic flows between $100M_{\odot}$ and $1,000M_{\odot}$. The thermal-pressure support is strongly dominant over the turbulent-pressure support in all four clumps. This is in contrast to the Jeans-unstable parent cloud, where the turbulent pressures are dominant.

Estimating the number density of SMS/DCBH formation sites. We estimate the co-moving number density n_{DCBH} of DCBH formation sites as $n_{\text{DCBH}} = n_{\text{ACH}} f_{\text{prim}} f_{\text{LW}} f_{\text{rapid}}$. Here, $n_{\text{ACH}} = 5.0 \pm 0.19$ per co-moving Mpc^3 is the co-moving number density of atomic-cooling haloes at redshift $z = 15$ (haloes above the mass threshold where cooling via atomic hydrogen is effective), $f_{\text{prim}} = 0.015 \pm 0.0045$ is the fraction of those haloes that are of primordial composition, $f_{\text{LW}} = 0.1 \pm 0.05$ is the fraction of the atomic-cooling haloes that are in regions where $f_{\text{LW}} \geq 3f_{21}$ (the fraction of the simulation volume above that flux threshold), and $f_{\text{rapid}} = 0.20 \pm 0.14$ is the fraction of the primordial atomic-cooling haloes that are

growing above the critical threshold where accretion heating is greater than cooling. On the basis of the quantities found in the rare-peak region of our simulation, we estimated these values and their variance, which are given in the main article. We then perform a Monte Carlo sampling of the parameter space. Extended Data Fig. 9 shows the cumulative probability of the expected DCBH number density in different large-scale environments. They steeply decrease above 10^{-3} , 10^{-6} and 10^{-9} DCBHs per co-moving Mpc^3 in the rare-peak, normal and void regions of the Renaissance simulations, respectively. The rare-peak has a median value of $n_{\text{DCBH}} = 1.1 \times 10^{-3}$ haloes per co-moving Mpc^3 , a 68% confidence interval of 1.9×10^{-4} – 2.8×10^{-3} haloes per co-moving Mpc^3 and a 95% confidence interval of 0 – 5.2×10^{-3} haloes per co-moving Mpc^3 .

When the same quantities are extracted from the normal and void simulation regions at $z = 15$, the median number density of DCBH haloes is expected to be about 10^{-7} haloes per co-moving Mpc^3 and 0 haloes per co-moving Mpc^3 , respectively, owing to the lack of atomic-cooling haloes of primordial composition and to a lack of atomic-cooling haloes that grow rapidly. The rare-peak region has a volume of 133.6 co-moving Mpc^3 (equivalent to a sphere of approximately $2.25/h$ co-moving Mpc in radius) and an average density of 1.65 times the cosmic mean. At $z = 15$, regions of that size and overdensity are expected to be found in approximately 0.01%–0.1% of the volume of the Universe, implying that a more realistic estimate of the global number density of DCBH candidates forming through this mechanism is in the range 10^{-7} – 10^{-6} haloes per co-moving Mpc^3 , consistent with our estimate in the normal region. This estimate is nonetheless approximately 100–1,000 times greater than the observed $z \approx 6$ quasar number density²⁷. Our results suggest that faint quasars at these high redshifts should be strongly clustered and associated with galaxy overdensities⁶⁸, providing an observational test of our proposed seeding mechanism. Furthermore, we find that DCBHs forming in this scenario have the same number density as the observed number density^{69,70} of present-day supermassive black holes above $10^8 M_\odot$. This abundance matching suggests that such central black holes in most elliptical galaxies have a common origin, beginning their lives as SMSs.

The fraction of rapidly growing atomic-cooling haloes. We compute an additional check on the fraction of rapidly growing haloes with the semi-analytic galaxy-formation code GalactiCus⁷¹. Most of the rare-peak region collapses into a halo with a total mass of $8.5 \times 10^{11} M_\odot$ at $z = 5$. We calculate 50 merger trees of equivalent $z = 5$ haloes that follow progenitor haloes as small as $3 \times 10^5 M_\odot$. Each merger tree has approximately 4×10^4 progenitor haloes at $z = 15$, totalling 2×10^6 progenitors in all of the calculated merger trees at this epoch. We find that 0.03% of haloes around the atomic-cooling threshold, $M_{\text{halo}} = (3\text{--}6) \times 10^7 M_\odot$, grow more than a factor of six between $z = 16$ and $z = 15$ (about 20 Myr). By using the halo descendant at a much later time, we can incorporate the effects of being in an overdense environment that lead to higher halo mass growth rates. This leads to a more accurate estimate when compared to randomly sampling atomic-cooling haloes at $z = 15$, the merger trees of which would be unlikely to be representative of our target haloes.

The metal-free haloes found in the Renaissance simulations. We searched and reported on the final output at $z = 15$ of the rare-peak region in the Renaissance simulation that satisfies the following criteria: (1) an atomic-cooling halo ($M_{\text{halo}} \geq 4.9 \times 10^7 M_\odot$ at $z = 15$); (2) contains only high-resolution dark-matter particles; (3) does not support metal or dust radiative cooling ($Z < 10^{-6} Z_\odot$); and (4) has no prior star formation. We consider the last criterion because some population III stars collapse directly into a stellar-mass black hole, producing no metals^{72,73}; however, because we randomly sample from an IMF, it is just as likely that the same population III star particle in question could have chemically enriched its host halo. Of 670 atomic-cooling haloes, ten fit these conditions (Extended Data Table 1). We also searched the normal and void regions and found no haloes matching the same criteria at $z = 15$. This suggests that SMS formation through this channel is much more likely in overdense regions of the early Universe. This crowded high-redshift environment lends itself to a high LW radiation field from more nearby galaxies and haloes with very high growth rates, existing in a medium with a higher average mass density. This null detection agrees with our statistical expectations.

We have so far focused on the MMH and LWH, but from the other eight haloes we gain insight into their variation. Eight of ten haloes experienced a growth rate per unit redshift greater than $10^{7.5} M_\odot$, showing that they grow from the minimum mass M_{crit} for molecular-hydrogen cooling to a mass that supports atomic cooling in less than a dynamical time (about 20 Myr). With the exception of one halo, all have a galaxy with a stellar mass of more than $10^6 M_\odot$ within 40 proper kpc. Stars in nearby galaxies create a boosted LW radiation field above $0.5 J_{21}$. Inspecting the central temperatures, we see that there are six cool-core ($T < 5,000$ K) haloes that have efficient H_2 cooling, with the other four haloes having warm cores. For various reasons, such as the LW radiation field and the degree of turbulence in the core⁴⁶, the warm-core haloes have their cooling suppressed at the final redshift of the simulation. However, this state is temporary, and the system will cool within a timescale defined by the ratio of the H_2 fraction and its formation rate as the haloes

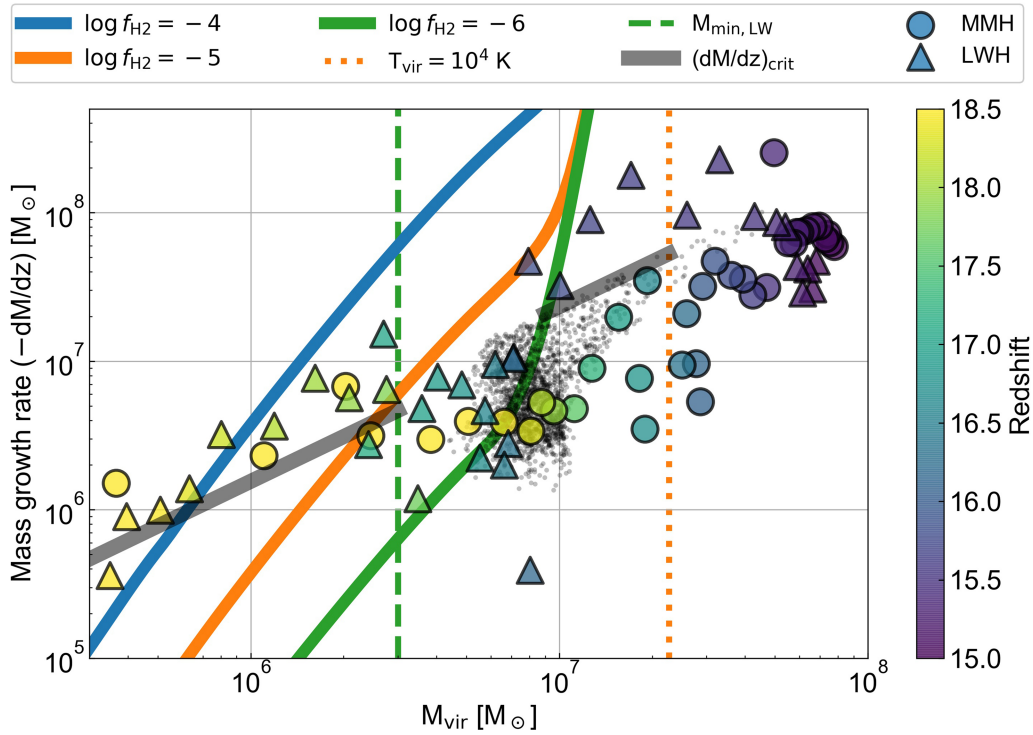
continue to grow⁴⁶. The higher core pressure limits the gravitational collapse, resulting in lower infall rates (less than $0.1 M_\odot \text{ yr}^{-1}$) compared to the cool-core haloes. The infall rates in our SMS candidates do not follow the usual thermal accretion rate (\dot{c}_s^3/G) because they have lost their thermal support in a short timescale relative to the free-fall time. Thus, they are experiencing their initial catastrophic collapse. Although SMS models have shown that a critical infall rate of $0.04 M_\odot \text{ yr}^{-1}$ is required, we include these warm-core haloes in our candidate list because molecular cooling and thus a further and more rapid collapse is inevitable⁷⁴. The halo with the highest infall rate (about $1 M_\odot \text{ yr}^{-1}$) is an interesting case because it is the farthest (124 proper kpc) from a galaxy and thus has the lowest J_{LW} in this sample. This halo also experiences the most rapid growth rate, which we attribute to it not collapsing earlier before it reaches the atomic-cooling limit. We note that the accretion rates given here are for a single snapshot, and the average accretion rate will vary as haloes undergo quiescent and intensive periods of cosmological accretion.

Data availability

The numerical experiments presented here were run with a hybrid OpenMP+MPI fork of the Enzo code, which is available from <https://bitbucket.org/jwise77/openmp>, using the changeset bcb436949d16. The data are publicly available from the Renaissance Simulation Laboratory at <http://girder.renslab.xyz>.

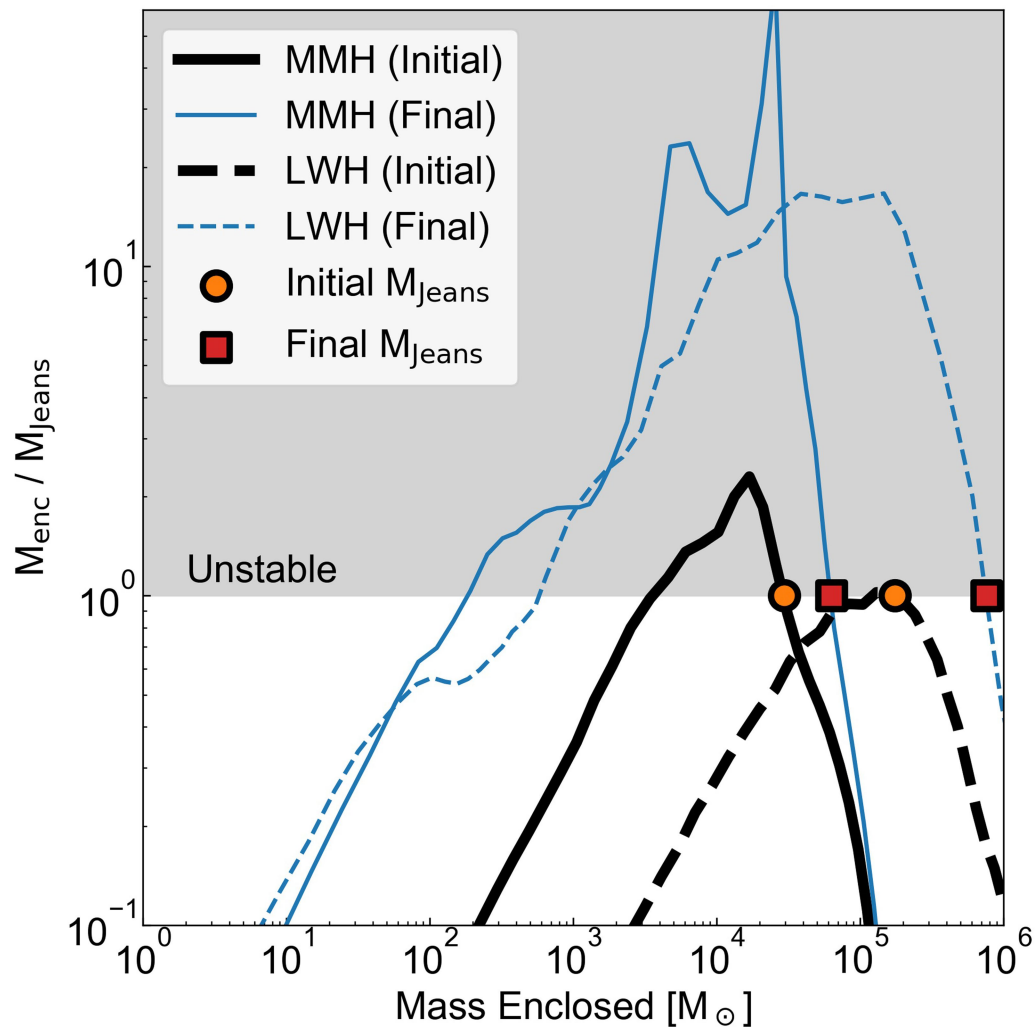
- Abel, T., Bryan, G. L. & Norman, M. L. The formation of the first star in the Universe. *Science* **295**, 93–98 (2002).
- O'Shea, B. W. & Norman, M. L. Population III star formation in a Λ CDM Universe. I. The effect of formation redshift and environment on protostellar accretion rate. *Astrophys. J.* **654**, 66–92 (2007).
- Turk, M. J., Abel, T. & O'Shea, B. The formation of population III binaries from cosmological initial conditions. *Science* **325**, 601–605 (2009).
- Xu, H., Wise, J. H. & Norman, M. L. Population III stars and remnants in high-redshift galaxies. *Astrophys. J.* **773**, 83 (2013).
- Xu, H., Ahn, K., Wise, J. H., Norman, M. L. & O'Shea, B. W. Heating the intergalactic medium by X-Rays from population III binaries in high-redshift galaxies. *Astrophys. J.* **791**, 110 (2014).
- Chen, P., Wise, J. H., Norman, M. L., Xu, H. & O'Shea, B. W. Scaling relations for galaxies prior to reionization. *Astrophys. J.* **795**, 144 (2014).
- Ahn, K., Xu, H., Norman, M. L., Alvarez, M. A. & Wise, J. H. Spatially extended 21 cm signal from strongly clustered UV and X-ray sources in the early Universe. *Astrophys. J.* **802**, 8 (2015).
- Xu, H., Norman, M. L., O'Shea, B. W. & Wise, J. H. Late pop III star formation during the epoch of reionization: results from the Renaissance simulations. *Astrophys. J.* **823**, 140 (2016).
- Komatsu, E. et al. Seven-year Wilkinson Microwave Anisotropy Probe (WMAP) observations: cosmological interpretation. *Astrophys. J. Suppl. Ser.* **192**, 18 (2011).
- Hahn, O. & Abel, T. Multi-scale initial conditions for cosmological simulations. *Mon. Not. R. Astron. Soc.* **415**, 2101–2121 (2011).
- Abel, T., Anninos, P., Zhang, Y. & Norman, M. L. Modeling primordial gas in numerical cosmology. *New Astron.* **2**, 181–207 (1997).
- Smith, B. D., Turk, M. J., Sigurdsson, S., O'Shea, B. W. & Norman, M. L. Three modes of metal-enriched star formation in the early Universe. *Astrophys. J.* **691**, 441–451 (2009).
- Behroozi, P. S., Wechsler, R. H. & Wu, H.-Y. The ROCKSTAR phase-space temporal halo finder and the velocity offsets of cluster cores. *Astrophys. J.* **762**, 109 (2013).
- Behroozi, P. S. et al. Gravitationally consistent halo catalogs and merger trees for precision cosmology. *Astrophys. J.* **763**, 18 (2013).
- Wise, J. H., Turk, M. J., Norman, M. L. & Abel, T. The birth of a galaxy: primordial metal enrichment and stellar populations. *Astrophys. J.* **745**, 50 (2012).
- Regan, J. A., Johansson, P. H. & Wise, J. H. Forming super-massive black hole seeds under the influence of a nearby anisotropic multi-frequency source. *Mon. Not. R. Astron. Soc.* **459**, 3377–3394 (2016).
- Wise, J. H. & Abel, T. Suppression of H_2 cooling in the ultraviolet background. *Astrophys. J.* **671**, 1559–1567 (2007).
- O'Shea, B. W. & Norman, M. L. Population III star formation in a Λ CDM Universe. II. Effects of a photodissociating background. *Astrophys. J.* **673**, 14–33 (2008).
- Naoz, S., Yoshida, N. & Gnedin, N. Y. Simulations of early baryonic structure formation with stream velocity. II. *The gas fraction*. *Astrophys. J.* **763**, 27 (2013).
- Regan, J. A., Johansson, P. H. & Wise, J. H. The effect of dark matter resolution on the collapse of baryons in high-redshift numerical simulations. *Mon. Not. R. Astron. Soc.* **449**, 3766–3779 (2015).
- Kitsionas, S. & Whitworth, A. P. Smoothed particle hydrodynamics with particle splitting, applied to self-gravitating collapse. *Mon. Not. R. Astron. Soc.* **330**, 129–136 (2002).
- Bromm, V. & Loeb, A. Formation of the first supermassive black holes. *Astrophys. J.* **596**, 34–46 (2003).
- Dotti, M., Colpi, M., Haardt, F. & Mayer, L. Supermassive black hole binaries in gaseous and stellar circumnuclear discs: orbital dynamics and gas accretion. *Mon. Not. R. Astron. Soc.* **379**, 956–962 (2007).
- Hirano, S. et al. One hundred first stars: protostellar evolution and the final masses. *Astrophys. J.* **781**, 60 (2014).

54. Chiaki, G. & Yoshida, N. Particle splitting in smoothed particle hydrodynamics based on Voronoi diagram. *Mon. Not. R. Astron. Soc.* **451**, 3955–3963 (2015).
55. Wolcott-Green, J., Haiman, Z. & Bryan, G. L. Photodissociation of H_2 in protogalaxies: modelling self-shielding in three-dimensional simulations. *Mon. Not. R. Astron. Soc.* **418**, 838–852 (2011).
56. Smith, B. D. et al. GRACKLE: a chemistry and cooling library for astrophysics. *Mon. Not. R. Astron. Soc.* **466**, 2217–2234 (2017).
57. Barkana, R. & Loeb, A. In the beginning: the first sources of light and the reionization of the Universe. *Phys. Rep.* **349**, 125–238 (2001).
58. Wise, J. H. & Abel, T. Resolving the formation of protogalaxies. I. Virialization. *Astrophys. J.* **665**, 899–910 (2007).
59. Wechsler, R. H., Bullock, J. S., Primack, J. R., Kravtsov, A. V. & Dekel, A. Concentrations of dark halos from their assembly histories. *Astrophys. J.* **568**, 52–70 (2002).
60. Regan, J. A. & Haehnelt, M. G. The formation of compact massive self-gravitating discs in metal-free haloes with virial temperatures of 13000–30000 K. *Mon. Not. R. Astron. Soc.* **393**, 858–871 (2009).
61. Wang, B. & Silk, J. Gravitational instability and disk star formation. *Astrophys. J.* **427**, 759–769 (1994).
62. Hartwig, T., Agarwal, B. & Regan, J. A. Gravitational wave signals from the first massive black hole seeds. *Mon. Not. R. Astron. Soc.* **479**, L23–L27 (2018).
63. Shu, F. H. Self-similar collapse of isothermal spheres and star formation. *Astrophys. J.* **214**, 488–497 (1977).
64. Bonnell, I. A., Bate, M. R. & Zinnecker, H. On the formation of massive stars. *Mon. Not. R. Astron. Soc.* **298**, 93–102 (1998).
65. Hosokawa, T., Yorke, H. W. & Omukai, K. Evolution of massive protostars via disk accretion. *Astrophys. J.* **721**, 478–492 (2010).
66. Woods, T. E., Heger, A., Whalen, D. J., Haemmerlé, L. & Klessen, R. S. On the maximum mass of accreting primordial supermassive stars. *Astrophys. J.* **842**, L6 (2017).
67. Chen, K.-J., Heger, A., Woosley, S., Almgren, A. & Whalen, D. J. Pair instability supernovae of very massive population III stars. *Astrophys. J.* **792**, 44 (2014).
68. Ota, K. et al. Large-scale environment of a $z = 6.61$ luminous quasar probed by $Ly\alpha$ emitters and Lyman break galaxies. *Astrophys. J.* **856**, 109 (2018).
69. Shankar, F. The demography of supermassive black holes: growing monsters at the heart of galaxies. *New Astron. Rev.* **53**, 57–77 (2009).
70. Terrazas, B. A. et al. Quiescence correlates strongly with directly measured black hole mass in central galaxies. *Astrophys. J.* **830**, L12 (2016).
71. Benson, A. J. GALACTICUS: a semi-analytic model of galaxy formation. *New Astron.* **17**, 175–197 (2012).
72. Heger, A., Fryer, C. L., Woosley, S. E., Langer, N. & Hartmann, D. H. How massive single stars end their life. *Astrophys. J.* **591**, 288–300 (2003).
73. Chatzopoulos, E. & Wheeler, J. C. Effects of rotation on the minimum mass of primordial progenitors of pair-instability supernovae. *Astrophys. J.* **748**, 42 (2012).
74. Visbal, E., Haiman, Z. & Bryan, G. L. A no-go theorem for direct collapse black holes without a strong ultraviolet background. *Mon. Not. R. Astron. Soc.* **442**, L100–L104 (2014).



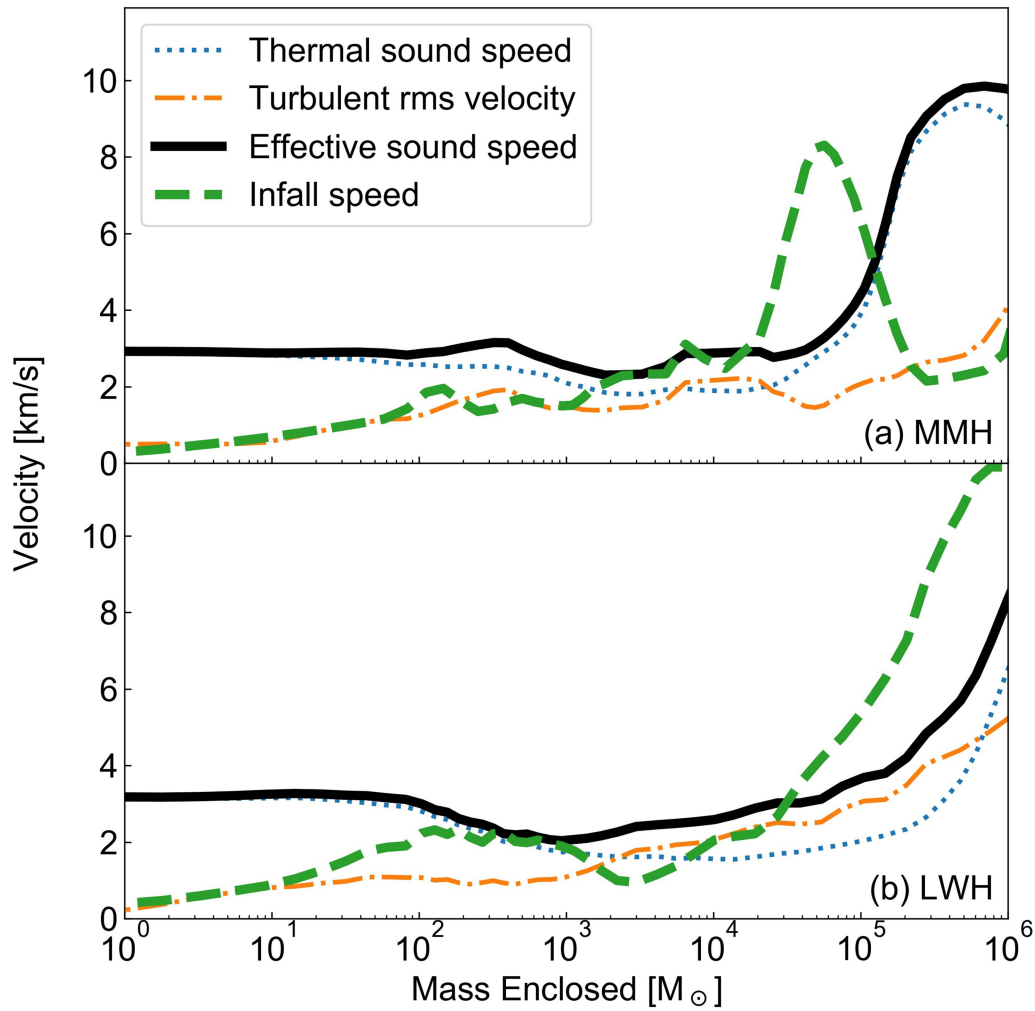
Extended Data Fig. 1 | Simulated and critical halo mass growth rates for SMS formation. A halo conducive for SMS formation must grow to the atomic-cooling limit ($2.2 \times 10^7 M_\odot$ at $z = 15$; orange dotted line) without hosting star formation or being chemically enriched from nearby galaxies. Haloes with masses below minimum mass $M_{\min, \text{LW}}$ (dashed green line) are suppressed by an external LW radiation field. Above this mass, haloes with sufficient dynamical heating to suppress radiative cooling grow above a critical rate (equation (1)), shown for H_2 number fractions f_{H_2} of 10^{-4} (blue solid line), 10^{-5} (orange solid line) and 10^{-6} (green solid line). The simulated growth rates of the MMH (circles) and LWH (triangles) are above the 10^{-6} rate once the halo masses pass $M_{\min, \text{LW}}$. Above a halo

mass of $8 \times 10^6 M_\odot$ (a virial temperature of 8,000 K at $z = 15$), dynamical heating will not suppress cooling because the atomic-radiative cooling rates are several orders of magnitude higher than the molecular ones. Both haloes grow rapidly to $M_{\min, \text{LW}}$, causing dynamical heating and preventing collapse for a sound-crossing time. The LWH grows from $8 \times 10^6 M_\odot$ to the atomic-cooling limit within a dynamical time of the central core. Both conditions set a critical growth rate (thick solid grey lines). All other atomic-cooling haloes (grey points) have similar growth rates between halo masses of $M_{\min, \text{LW}}$ and $8 \times 10^6 M_\odot$ but far short of the critical growth rate. Nearly all of these haloes cool and form stars before reaching the atomic-cooling limit.



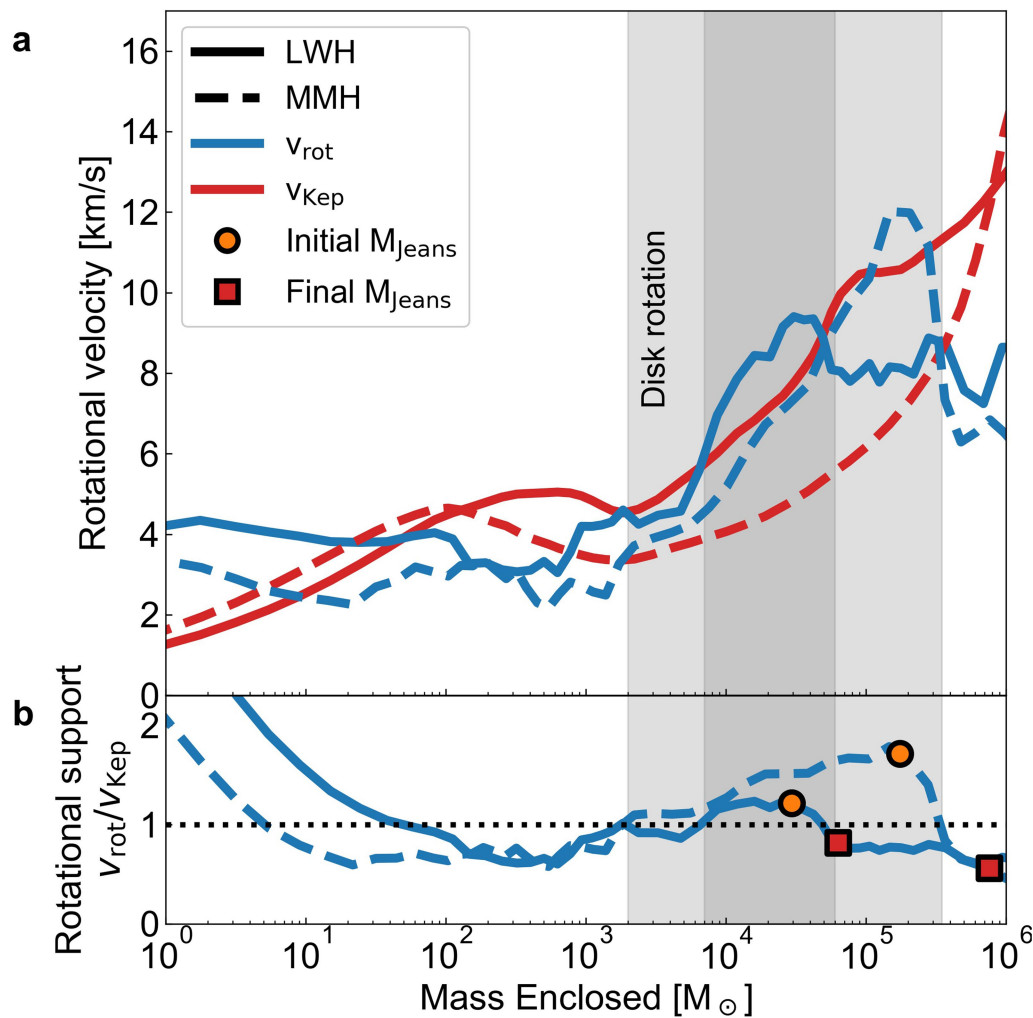
Extended Data Fig. 2 | Gravitational instability of the growing core. The ratio of the enclosed gas mass M_{enc} and the Jeans mass M_{Jeans} as a function enclosed gas mass is shown for the MMH (solid lines) and the LWH (dashed lines) when each halo first becomes gravitationally unstable (thick

black lines), that is, when $M_{\text{enc}}/M_{\text{Jeans}} \geq 1$ (shaded region), and in the final simulation state (thin blue lines). The orange circles and red squares indicate the mass scale of the collapsing gas cloud that is co-located with the centre of the host halo.



Extended Data Fig. 3 | Thermal and turbulent support of the collapsing core. a, b, Gravitational forces dominate over thermal and turbulent internal pressures within the collapsing core in the MMH (a) and the LWH (b). The thermal sound speed (blue dotted lines) and turbulent root-mean-square velocity (orange dash-dotted line) both contribute to

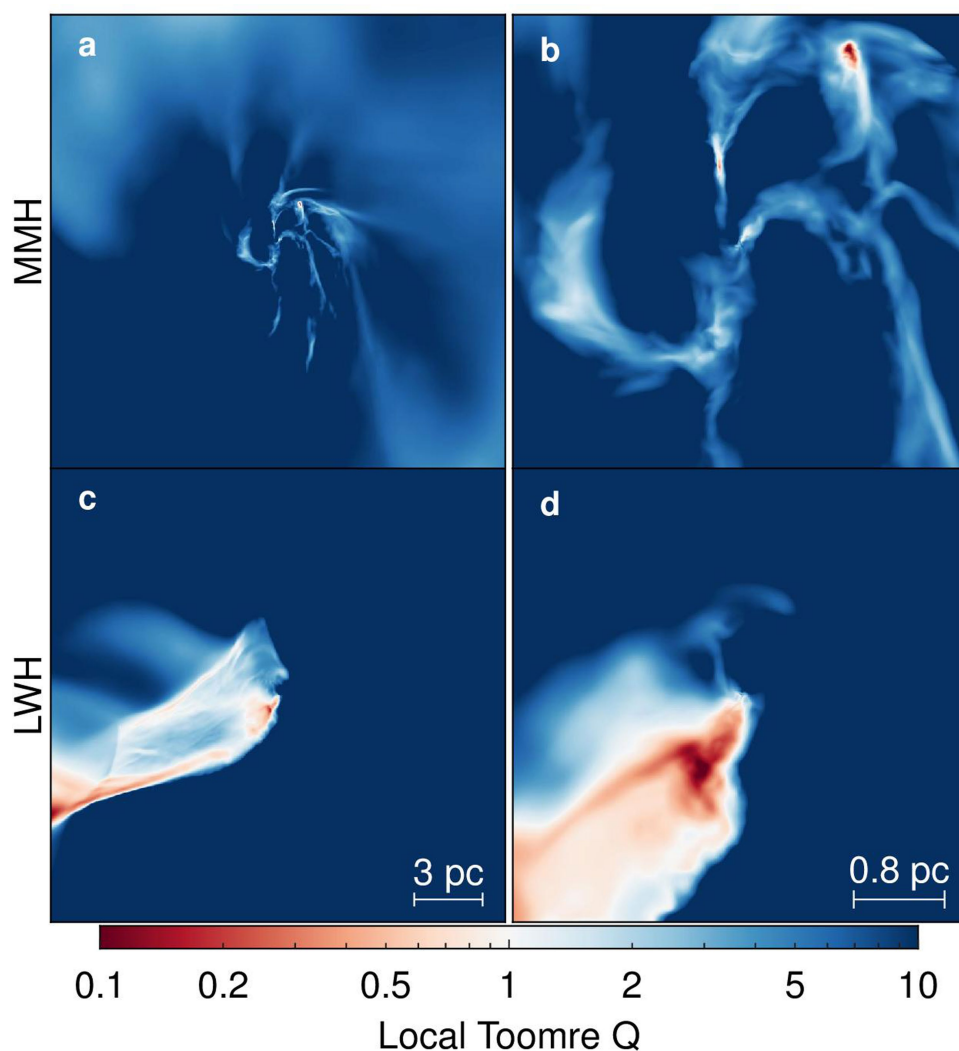
the effective sound speed (black solid line) that provides partial resistance to a catastrophic collapse. The radial infall speed (green dashed line) shows that the flow becomes supersonic at the Jeans mass scale and then transitions to a subsonic flow at smaller mass scales. In the LWH, the radial inflow becomes transonic at a mass scale of $10^3 M_{\odot}$.



Extended Data Fig. 4 | Rotational properties of the target haloes.

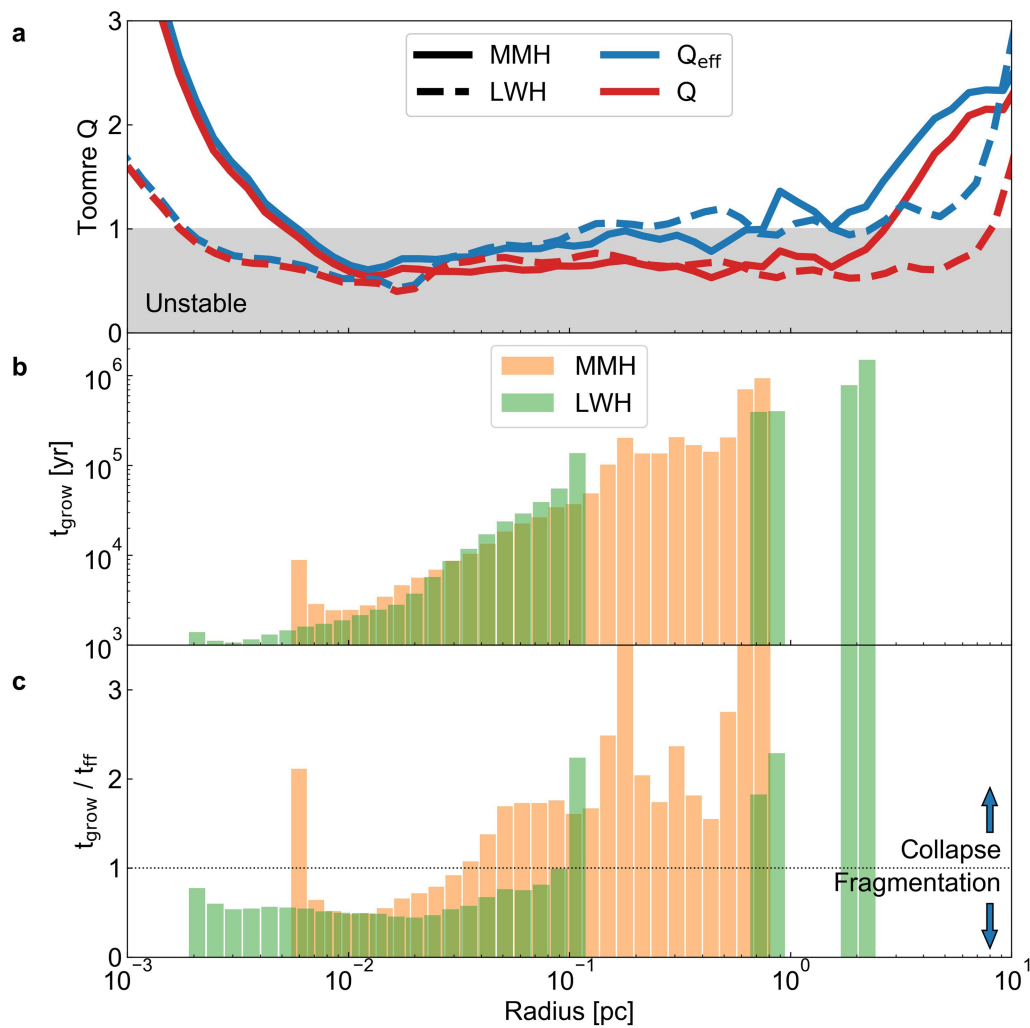
a, Radially averaged profiles of circular velocity $v_{\text{Kep}} = \sqrt{GM/r}$ (red lines) and rotational velocity v_{rot} (blue lines) around the largest principal axis of the MMH (dashed lines) and the LWH (solid lines) at the end of the simulation. **b**, Radially averaged profiles of the fractional rotational support; a ratio greater than one indicates that rotational velocities are sufficient to prevent gravitational collapse. The shaded regions show where the systems are rotationally supported: $2 \times 10^3 M_{\odot}$ – $3.3 \times 10^3 M_{\odot}$ for

the MMH (light shading) and $7 \times 10^3 M_{\odot}$ – $6 \times 10^4 M_{\odot}$ for the LWH (dark shading). Rotation works in tandem with thermal and turbulent pressures to marginally slow the collapse, seen in the lower infall speeds at these mass scales in Extended Data Fig. 3. Inside $100 M_{\odot}$, this rotational measure becomes ill-defined because the rotation centre and centre-of-mass are not co-located; thus, we do not conclude that the inner portions are rotationally supported even though $v_{\text{rot}}/v_{\text{Kep}} > 1$.



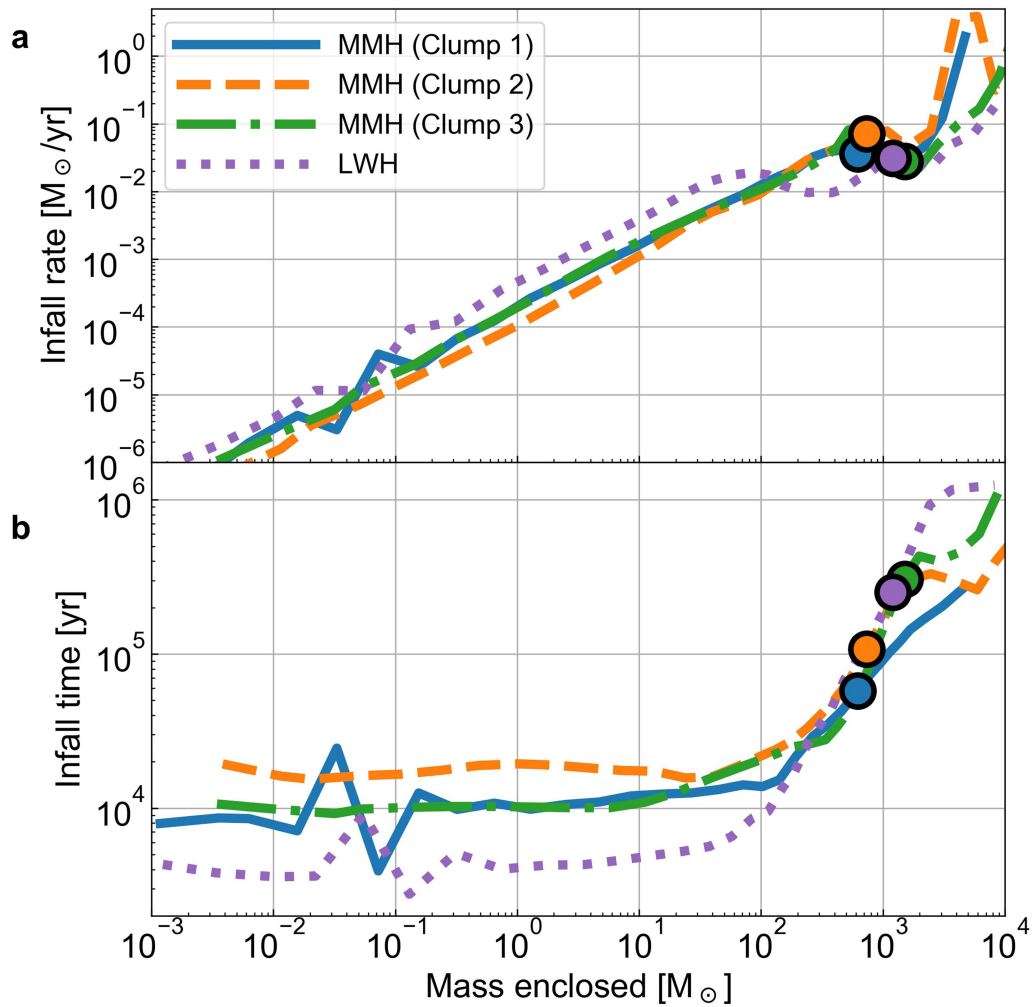
Extended Data Fig. 5 | Distribution of fragmentation-prone regions. **a–d**, Density-weighted projections of a local estimate of the Toomre Q parameter (equation (2)) for the MMH (**a**, **b**) and the LWH (**c**, **d**) in a field of view of 20 pc (left) and 4 pc (right), centred on the densest point and aligned to be perpendicular with the angular momentum vector of the disk. A value greater than one indicates that rotation and internal pressure stabilizes regions against fragmentation into smaller self-gravitating

objects. In the MMH, this analysis highlights the clump fragments with the filaments being only marginally stable at $Q \approx 1$. The sheet in the LWH that formed from a preceding major halo merger is apparent in this measure. The bulk of the sheet is only marginally stable, with the edge and collapsing centre containing an environment that is conducive to fragmentation.



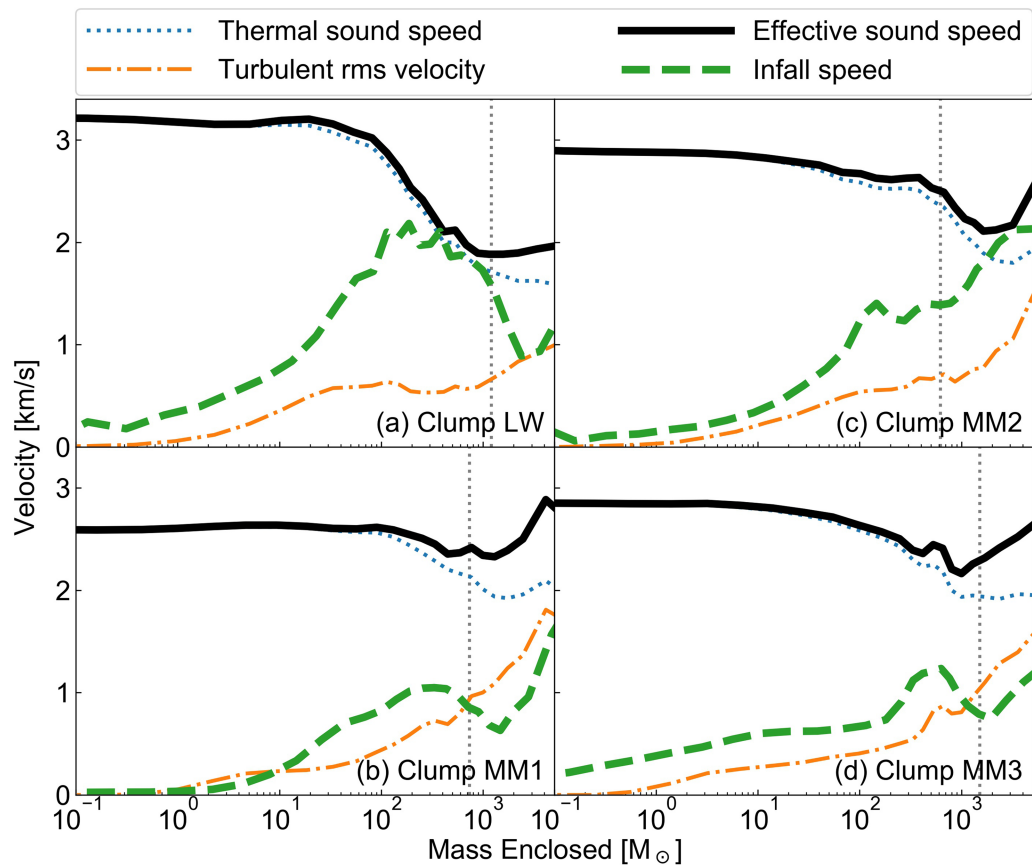
Extended Data Fig. 6 | Growth rates for fragmentation. A rotating system will fragment into self-gravitating clumps only when the growth rates of the density perturbations are faster than the collapse timescale. **a**, Cylindrical radial profiles of Q when considering only thermal support (red) and with thermal and turbulent support (blue), for the MMH (dashed) and the LWH (solid). The shaded region indicates where the system is unstable to fragmentation. **b**, The unstable regions have a characteristic growth rate, defining a growth timescale t_{grow} , which

exhibits an increasing trend with radius for the MMH (orange) and the LWH (green). **c**, If the ratio of t_{grow} and the free-fall time t_{ff} is less than one, the region can fragment before it gravitationally collapses. In the MMH, this condition is true at radii less than 0.03 pc, indicating that small-scale fragmentation might occur but will subsequently be suppressed by a rapid monolithic collapse. The LWH exhibits this feature inside 0.1 pc but is surrounded by gas that is stable against fragmentation.



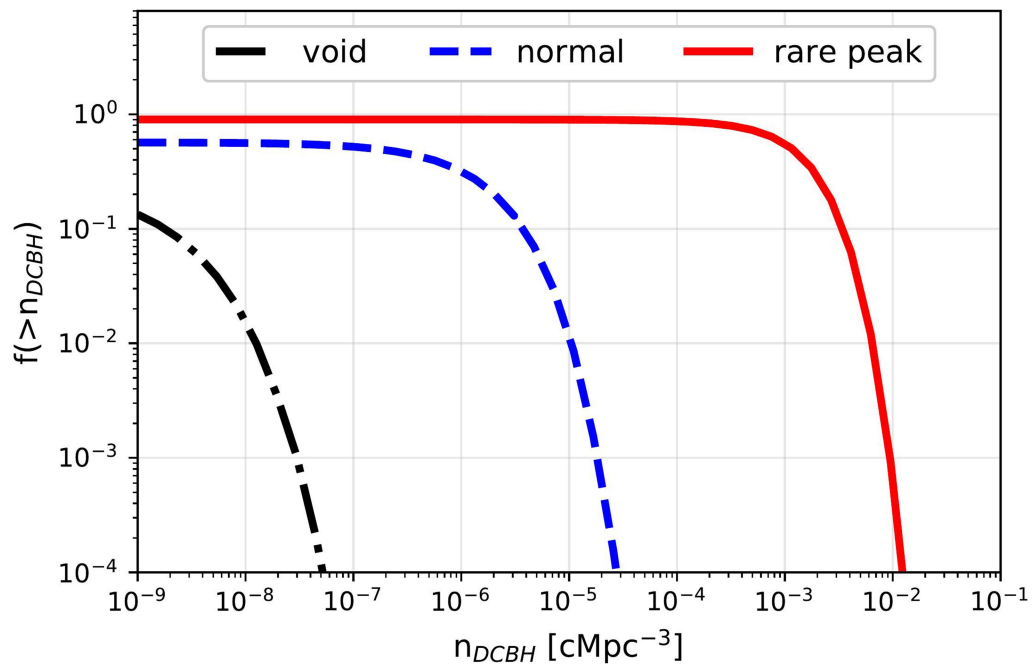
Extended Data Fig. 7 | Clump infall rates and timescales. Similar to the results presented in Fig. 4d, the self-gravitating clumps are growing through radial infall. **a**, The infall rates are computed as the mass flux through spherical shells and steadily increase with enclosed mass. The rate in the single clump of the LWH (dotted purple line) is more than a factor three greater than the three major clumps in the MMH. The circles mark the infall rate at the clump mass. **b**, The infall time, the ratio of the

mass enclosed and infall rate, is an informative scale that can be used to compare against star-formation timescales. This timescale is constant and approximately 10 kyr within $100M_{\odot}$ for all clumps and rises to about 100 kyr for the entire clump, marked by the circles. This rapid infall suggests that sufficient mass will collapse into the supermassive protostar before it reaches main-sequence.



Extended Data Fig. 8 | Thermal and turbulent support of collapsing clumps. a–d, Same as Extended Data Fig. 3, but for the clumps in the LWH (a) and the MMH (b–d). The vertical dotted lines mark the clump mass. The radial inflows are subsonic for all four clumps, but the clump in LWH

contains transonic flows between $100M_{\odot}$ and $1,000M_{\odot}$. Thermal support is dominant inside the clumps, unlike the larger parent Jeans-unstable system, where turbulent effective pressures are comparable to their thermal counterparts (see Extended Data Fig. 3).



Extended Data Fig. 9 | Abundance estimate of DCBHs. The cumulative probability of the co-moving number density of haloes that potentially host supermassive star formation is shown for the rare-peak (red solid line), normal (blue dashed line) and void (black dash-dotted line) regions of the Renaissance simulations. Their respective median number densities

are 1.1×10^{-3} , about 10^{-7} and 0 haloes per co-moving Mpc^3 . Subsequent DCBH formation is most likely to occur in overdense regions of the early Universe, whereas few or no haloes will form in average and underdense regions.

Extended Data Table 1 | Properties of halo candidates hosting supermassive star formation

$\log_{10}(M_{\text{halo}})$ [M_{\odot}]	$\log_{10}(\text{mean Growth rate})$ [M_{\odot} per unit redshift]	J_{LW}/J_{21}	D_{gal} [kpc]	T_{c} [K]	Gas infall rate [M_{\odot}/yr]
7.84*	7.78	2.71	12.7	2250	0.275
7.76 [†]	7.53	3.23	11.8	4390	0.171
7.76	7.76	1.91	14.7	4220	0.286
7.75	7.65	0.583	35.5	1730	0.290
7.75	7.39	0.958	19.7	7570	0.0294
7.74	7.88	1.49	25.0	8670	0.0574
7.73	7.79	0.894	29.9	1760	0.396
7.70	7.22	2.62	18.3	6520	0.0292
7.67	7.90	0.16	124	1080	1.05
7.64	7.78	2.14	6.20	7890	0.0356

The growth rate is averaged over the last 20 Myr of the simulation. The values of J_{LW} and of the gas temperature T_{c} are given at the densest point. D_{gal} is the distance to the nearest galaxy with at least $10^6 M_{\odot}$ of stars. The gas infall rate is the mass-averaged value within 100 pc. All data are given at $z = 15$ from the original Renaissance simulation of the rare-peak region.

*MMH.

[†]LWH.